Joint inversion of co-seismic and early post-seismic slip to optimize the information content in geodetic data: Application to the 2009 M_W6.3 L'Aquila earthquake, Central Italy

Théa Ragon[1], **Anthony Sladen**[1], **Quentin Bletery**[1], **Mathilde Vergnolle**[1], **Olivier Cavalié**[1], **Antonio Avallone**[2]

[1]Université Côte d'Azur, CNRS, IRD, Observatoire de la Côte d'Azur, Géoazur, Valbonne, France
[2]Istituto Nazionale di Geofisica e Vulcanologia, Rome, Italy

Key Points:

- Simultaneous inversion of geodetic data with different spatio-temporal resolution maximizes the information content
- Incorporating early afterslip deformation when solving for the co-seismic processes (as with InSAR data) overestimate inferred co-seismic models
- Estimations of the post-seismic processes neglecting early afterslip deformation may largely underestimate the total afterslip amplitude

Corresponding author: Théa Ragon, ragon@geoazur.unice.fr

Abstract

When analyzing the rupture of a large earthquake, geodetic data are often critical. These data are generally characterized by either a good temporal or a good spatial resolution, but rarely both. As a consequence, many studies analyze the co-seismic rupture with data also including one or more days of early post-seismic deformation. Here, we propose to invert simultaneously for the co- and post-seismic slip with the condition that the sum of the two models remains compatible with data covering the two slip episodes. We validate the benefits of our approach with a toy model and an application to the 2009 M_w6.3 L'Aquila earthquake, using a Bayesian approach and accounting for epistemic uncertainties. For the L'Aquila earthquake, we find that if early post-seismic deformation is acknowledged as co-seismic signal, co-seismic slip models may overestimate the peak amplitude while long-term post-seismic models may largely underestimate the total post-seismic slip amplitude. This example illustrates how the proposed approach could improve our comprehension of the seismic cycle, of the fault frictional properties, and how the co-seismic rupture, afterslip and aftershocks relate to one another.

1 Introduction

The occurrence of earthquakes and seismic sequences is mainly controlled by the spatial and temporal evolution of crustal stresses. The co-seismic stress change and the redistribution of stress following an earthquake thus both play an important role in the seismic cyle and the mechanical behavior of faults, including the generation of new seismic sequences. To understand both co-seismic and post-seismic processes, and their relationship, is thus a crucial step to propose realistic earthquakes scenario and reliable hazards estimates.

While earthquakes can last for a few seconds to minutes, their post-seismic stress relaxation can last months to years. Post-seismic relaxation is generally modeled by several interacting mechanisms, such as localized shear on the fault (a.k.a. afterslip) [e.g. *Marone et al.*, 1991; *Freed*, 2007; *Johnson et al.*, 2012], viso-elastic deformation in the lower crust or mantle [e.g. *Nur and Mavko*, 1974; *Pollitz et al.*, 1998; *Freed and Burgmann*, 2004] or poroelastic rebound [e.g. *Peltzer et al.*, 1998; *Jonsson et al.*, 2003]. The interactions between co-seismic stress changes, aftershocks and post-seismic deformation are still poorly understood [e.g. *Perfettini and Avouac*, 2007]. Slip on the fault may be governed by two brittle deformation modes following rate and state friction laws [*Rice and L. Ruina*, 1983]: seismic rupture may occur in velocity weakening area, whereas afterslip may develop in the velocity strengthening zone [e.g. *Marone et al.*, 1991]. In contrast, *Helmstetter and Shaw* [2009] also show that afterslip processes may be primarily driven by stress heterogeneities, independently of the rate and state friction behavior. Aftershocks may be triggered by co-seismic stress changes, without direct relation with post-seismic deformation [*Dieterich*, 1994]. Or, aftershocks may also be primarily triggered by the post-seismic reloading due to afterslip [e.g. *Perfettini and Avouac*, 2004; *Hsu et al.*, 2006; *Peng and Zhao*, 2009; *Ross et al.*, 2017]. The variability of these theories emphasizes the need to refine our comprehension and description of the co-seismic and post-seismic phases and their transition.

Our understanding of the co-seismic processes mainly derives from modeling of seismic, geodetic and tsunami data, and our understanding of post-seismic behaviors is mainly improved with the modeling of geodetic observations [e.g. *Burgmann et al.*, 1997; *Wang et al.*, 2012; *Perfettini and Avouac*, 2014; *Gualandi et al.*, 2017] or simulation [e.g. *Smith and Sandwell*, 2004; *Barbot and Fialko*, 2010; *Cubas et al.*, 2015]. The observations thus remain a cornerstone to identify and characterize the co- and post-seismic processes. GNSS time series are commonly used and can provide a good temporal resolution. But the spatial resolution of such observation is usually limited. In contrast, synthetic aperture radar interferometry (InSAR) can provide extensive spatial coverage but with a limited temporal resolution. Indeed, while earthquakes last for a few seconds, very often satellites have a revisit time of more than a few days. If earthquakes do not nucleate just before the visit of a satellite, which is generally the case, the measured deformation is the co-seismic signal plus a fraction of the post-seismic deformation. As a consequence, most earthquakes models based on geodetic observations are biased by unwanted deformation signal. In practice, used interferograms or campaign GNSS offsets generally cover time periods extending at least a few days before and after the mainshock. Pre-earthquake signals, when evidenced, are usually related to small slip episodes at depth near the hypocenter. The associated surface deformation signals are usually hard to detect and neglected in co-seismic studies. The post-seismic deformation happening on the first few days after the mainshock is usually detectable in the geodetic data but incorporated in source estimation problems as if it was part of the co-seismic signal [e.g. *Elliott et al.*, 2013; *Lin et al.*, 2013; *Cheloni et al.*, 2014; *Bletery et al.*, 2016; *He et al.*, 2017; *Salman et al.*, 2017; *Barnhart et al.*, 2018], with the justification that it is comparatively small. Similarly, post-seismic models generally do not account for observations related to the early post-seismic deformation because they are often contaminated by co-seismic signal [e.g. *D'Agostino et al.*, 2012; *Cheloni et al.*, 2014]. What we name here the early post-seismic phase corresponds to the overlooked part of the post-seismic deformation, and can last for a few hours after the mainshock in the best case, or a few days in most studies. Yet, the largest post-seismic deformation rate is expected during the first few days after the mainshock, considering that its main trend is to decrease exponentially with time after an earthquake.

The early post-seismic processes remain largely unexplored, because of the limited temporal and spatial resolution of geodetic data. Neglecting the early post-seismic signal may also affect our understanding of both co-seismic and post-seismic processes. And this effect is probably persisting if seismic data (i.e. purely co-seismic) are added to the inverse problem, since geodetic data tend to have a stronger control on the inferred distribution of slip, at least in the first 10 km below the Earth surface [e.g. *Delouis et al.*, 2002].

The recent advent of high-frequency GNSS has allowed to record the strictly co-seismic signal (10 to 30 seconds after the earthquake time occurrence) without any contamination by early post-seismic deformation. Well instrumented earthquakes are thus now characterized by at least two geodetic datasets, one being strictly co-seismic and the other which also includes some days of early afterslip. In this study, we use an original inversion methodology to jointly infer co-seismic and early post-seismic slip models, taking advantage of the complementary spatial and temporal resolutions of different geodetic observations. We first validate the approach through a toy model, and then analyze and illustrate the benefits of our methodology with a real event. We consider the 2009 M_w6.3 L'Aquila earthquake, Central Italy, which has been intensively studied but whose very early post-seismic phase has not been imaged. The choice of the L'Aquila event is also motivated by the large density of near field observations and the overall quality of the instrumentation. Additionally, this event ruptured a relatively well known and simple fault geometry, in an area where crustal properties have been investigated in detail: this will ensure the forward physics and its uncertainties can be estimated. In this work we investigate the impact of accounting for early afterslip on co-seismic models. We explore the impact of uncertainties in the slip imagery with a probabilistic approach and account for uncertainties in the physics of our problem. The results will allow us to investigate the relationship between co-seismic rupture, early afterslip processes, longer term afterslip and the distribution of aftershocks.

2 Inversion Framework

2.1 Dual time inversion of co-seismic and early post-seismic data

For a number of earthquakes, we have the opportunity to use two static datasets: one which is strictly co-seismic ("co") and the other which contains co-seismic and early post-seismic signal ("co+post"). To infer the strictly co-seismic and early post-seismic slip distributions, one approach could be to invert separately for the two datasets, and assume that the strictly post-seismic ("post") solution is the difference between the "co" and "co+post" models. However, in this case, the model "co" would be constrained by fewer observations (only few GNSS offsets), most of the co-seismic information being in the "co+post" dataset (dense map of InSAR offsets). An alternative approach is to assume that the "co+post" slip model is the sum of the "co" and "post" slip distributions. We then have:

$$\begin{cases} \mathbf{d}_{\text{co}} = \mathbf{G}_{\text{co}}^{\text{co}} \cdot \mathbf{m}_{\text{co}} \\ \mathbf{d}_{\text{co+post}} = \mathbf{G}_{\text{co+post}}^{\text{co}} \cdot \mathbf{m}_{\text{co}} + \mathbf{G}_{\text{co+post}}^{\text{post}} \cdot \mathbf{m}_{\text{post}} \end{cases} \tag{1}$$

where matrices of the Green's functions $\mathbf{G}_{\text{data}}^{\text{model}}$ have been calculated for the corresponding dataset and model. For instance, $\mathbf{G}_{\text{co+post}}^{\text{co}}$ is the matrix of the Green's functions calculated from the model "co" for the data "co+post". The Eq. 1 can also be represented in the following matrix form:

$$\begin{pmatrix} \mathbf{d}_{\text{co}} \\ \mathbf{d}_{\text{co+post}} \end{pmatrix} = \begin{pmatrix} \mathbf{G}_{\text{co}}^{\text{co}} & 0 \\ \mathbf{G}_{\text{co+post}}^{\text{co}} & \mathbf{G}_{\text{co+post}}^{\text{post}} \end{pmatrix} \cdot \begin{pmatrix} \mathbf{m}_{\text{co}} \\ \mathbf{m}_{\text{post}} \end{pmatrix}. \tag{2}$$

The redesigned Green's functions matrix is now composed of 3 sub-matrices. As we focus on the early post-seismic phase, we can make the assumption that both $\mathbf{G}_{\text{co+post}}^{\text{co}}$ and $\mathbf{G}_{\text{co+post}}^{\text{post}}$ matrices are identical because we suppose both co-seismic and early post-seismic deformations are elastic. We can thus write

$$\begin{pmatrix} \mathbf{d}_{\text{co}} \\ \mathbf{d}_{\text{co+post}} \end{pmatrix} = \begin{pmatrix} \mathbf{G}_{\text{co}} & 0 \\ \mathbf{G}_{\text{co+post}} & \mathbf{G}_{\text{co+post}} \end{pmatrix} \cdot \begin{pmatrix} \mathbf{m}_{\text{co}} \\ \mathbf{m}_{\text{post}} \end{pmatrix}. \tag{3}$$

If strictly post-seismic observations are available, we could also incorporate these data into our equation to help constrain the "post" model:

$$\begin{pmatrix} \mathbf{d}_{\text{co}} \\ \mathbf{d}_{\text{co+post}} \\ \mathbf{d}_{\text{post}} \end{pmatrix} = \begin{pmatrix} \mathbf{G}_{\text{co}}^{\text{co}} & 0 \\ \mathbf{G}_{\text{co+post}}^{\text{co}} & \mathbf{G}_{\text{co+post}}^{\text{post}} \\ 0 & \mathbf{G}_{\text{post}}^{\text{post}} \end{pmatrix} \cdot \begin{pmatrix} \mathbf{m}_{\text{co}} \\ \mathbf{m}_{\text{post}} \end{pmatrix}, \tag{4}$$

with $\mathbf{G}_{\text{post}}^{\text{post}}$ reflecting the response of the Earth for the strictly post-seismic data. The "post" dataset then corresponds to the same post-seismic time window as what is covered by the "co+post" dataset.

The off-diagonal terms of the redesigned Green's function matrix allow us to make use of the "co+post" dataset to constrain both "co" and "post" models. In the following, we refer to this approach as Combined Time Windows (CTW) approach. The CTW approach can be generalized to cover various intervals of post-seismic deformation. Indeed, while for many earthquakes strictly co-seismic data are now available, non-strictly co-seismic datasets usually cover variable time intervals. If, for instance, two intervals of post-seismic deformation contaminate the co-seismic signal, with only one of these intervals observed independently, our equation 3 can be adapted as

$$\begin{pmatrix} \mathbf{d}_{\text{co}} \\ \mathbf{d}_{\text{co+post1}} \\ \mathbf{d}_{\text{co+post2}} \\ \mathbf{d}_{\text{post2}} \end{pmatrix} = \begin{pmatrix} \mathbf{G}_{\text{co}}^{\text{co}} & 0 & 0 \\ \mathbf{G}_{\text{co+post1}}^{\text{co}} & \mathbf{G}_{\text{co+post1}}^{\text{post1}} & 0 \\ \mathbf{G}_{\text{co+post2}}^{\text{co}} & \mathbf{G}_{\text{co+post2}}^{\text{post1}} & \mathbf{G}_{\text{co+post2}}^{\text{post2}} \\ 0 & 0 & \mathbf{G}_{\text{post2}}^{\text{post2}} \end{pmatrix} \cdot \begin{pmatrix} \mathbf{m}_{\text{co}} \\ \mathbf{m}_{\text{post1}} \\ \mathbf{m}_{\text{post2}} \end{pmatrix}, \tag{5}$$

with $\mathbf{d}_{\text{post2}}$ reflecting the surface displacement for the time interval between times 1 and 2, and $\mathbf{G}_{\text{post2}}^{\text{post2}}$ and $\mathbf{m}_{\text{post2}}$ associated Green's functions and slip model. Indeed, this approach could be used to investigate as many time windows of post-seismic deformation as needed.

To refine co-seismic models and investigate early post-seismic deformation of the L'Aquila earthquake, we follow here the approach described by Eqs 1 and 3. We do not incorporate any information on the strictly post-seismic phase to investigate the very simple case where only co-seismic data (contaminated or not by early post-seismic deformation) are available.

2.2 Accounting for Epistemic Uncertainties

When imaging a slip distribution on a fault, the physics of the forward model is usually assumed of minimum complexity to simplify the computation and also often because we don't know well the Earth interior. For instance, Earth interior is frequently approximated as an elastic and homogeneous environment and the causative fault geometry is usually reduced to a flat rectangular plane. The uncertainties related to our approximations of the physics of the Earth affect the inferred source models [*Ragon et al.*, 2018]. As the early post-seismic slip is of limited amplitude, it may be particularly impacted by uncertainties of the forward model. We thus account for epistemic uncertainties following the approach developed by *Duputel et al.* [2014] for the Earth elastic properties and *Ragon et al.* [2018] for the fault geometry. The epistemic uncertainties are calculated from the sensitivity of the Green's Functions and are included in a covariance matrix $\mathbf{C}_\mathrm{p}$.

2.3 Bayesian approach

Our inverse problem solves for both co-seismic and early post-seismic slip parameters, the later being of limited amplitude. While the co-seismic parameters will be reasonably well constrained, multiple early post-seismic models will probably be realistic. To get a robust image of the early post-seismic phase, we thus solve our problem with a Bayesian sampling approach which relies on the AlTar package, which is a rewrite of the code CATMIP [*Minson et al.*, 2013]. AlTar combines the Metropolis algorithm with a tempering process to realize an iterative sampling of the solution space of the source models. A large number of samples are tested in parallel at each transitional step. Additionally, a resampling is performed at the end of each step to replace less probable models. The probability of each sample to be selected depends on its ability to fit the observations $\mathbf{d}_\mathrm{obs}$ within the uncertainties $\mathbf{C}_\chi = \mathbf{C}_\mathrm{d} + \mathbf{C}_\mathrm{p}$, with $\mathbf{C}_\mathrm{d}$ the observational errors and $\mathbf{C}_\mathrm{p}$ the epistemic uncertainties.

The ability of each model parameter to solve the source problem is evaluated through repeated updates of the probability density functions (PDFs)

$$f(\mathbf{m}, \beta_i) \propto p(\mathbf{m}) \cdot \exp[-\beta_i \cdot \chi(\mathbf{m})], \tag{6}$$

where $\mathbf{m}$ is the current sample, $p(\mathbf{m})$ is the prior information on this sample, i corresponds to each iteration and β evolves dynamically from 0 to 1 to ensure an exhaustive exploration of the solution space [*Minson et al.*, 2013]. $\chi(\mathbf{m})$ is the misfit function:

$$\chi(\mathbf{m}) = \frac{1}{2}[\mathbf{d}_\mathrm{obs} - \mathbf{G} \cdot \mathbf{m}]^T \cdot \mathbf{C}_\chi^{-1} \cdot [\mathbf{d}_\mathrm{obs} - \mathbf{G} \cdot \mathbf{m}]. \tag{7}$$

The use of AlTar with the CTW approach allows us to specify prior information on each model, and thus to ensure the non-negativity of both co-seismic and post-seismic slip models (or of any time window model).

3 Application to a simplified 2D model

To ensure that our methodology allows to reliably infer the slip distribution of different time windows, we first analyze a synthetic 2D case where the slip is imaged either

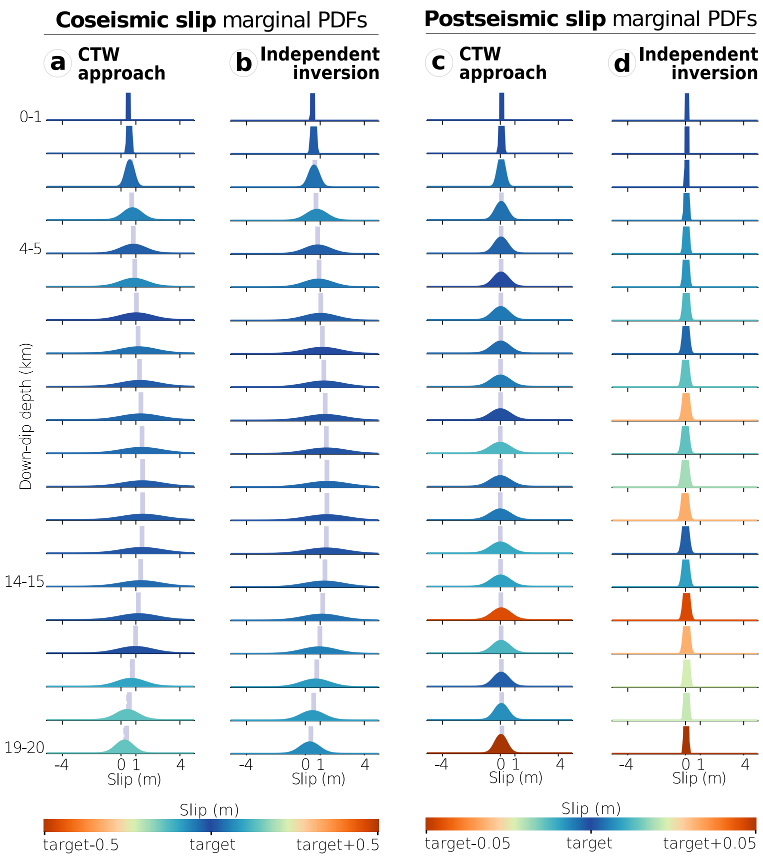

Figure 1. Co-seismic and post-seismic slip inferred for the simplified case of a fault that extends infinitely along strike. The co- and post-seismic slip models inferred from the CTW approach are shown in (a) and (c), and can be compared to the slip inferred from the inversion of co-seismic data only (b) and the post-seismic slip distribution (d) resulting from the difference between slip inferred from the inversion of co+post data and slip of (b). The fault is discretized along dip in 20 subfaults, for which are represented the target parameters as gray vertical lines. For each subfault, the posterior PDFs of co-seismic (a and b) and post-seismic (c and d) slip is colored according to the offset between the target parameter and the posterior mean, with a colorscale saturated at 50 cm for the co-seismic slip and at 5 cm for the post-seismic slip. The target slip is well inferred if the PDF of a particular parameter is colored in dark blue, while it is not if the PDF is colored in red.

independently or with the CTW approach. For this simple case, we assume two time windows named for the purpose of simplicity co-seismic and post-seismic.

3.1 Forward Model

We assume a fault extending infinitely along strike and which is 20 km wide along dip. The fault is discretized along dip into sub-faults of 1 km width and is dipping 55°. We assume the co-seismic slip on this fault to be purely dip-slip and to vary gradually with depth between 0 m and 1.5 m, with maximum slip between 9 and 14 km depth. We also assume that there is post-seismic slip on the same fault, with a similar location and direction and an amplitude equal to a tenth of the co-seismic slip amplitude. We compute the corresponding "co" and "co+post" synthetic observations using the expressions of surface displacement in an homogeneous elastic half-space [*Segall*, 2010]. These synthetic observations are computed for 100 data points at the surface, spaced every kilometer. A correlated Gaussian noise of 5 mm is added to the synthetic data to simulate measurement errors. Note that, for this toy model, the number of "co" data is the same as the number of "co+post" observations.

Using these 100 synthetic observation points, we then estimate the depth distribution of slip still assuming a homogeneous elastic half-space. We use a uniform prior distribution $p(\mathbf{m}) = \mathcal{U}(-0.5 \text{ m}, 5 \text{ m})$ for the dip slip component (uniform implies that all values are considered equally likely with no a priori knowledge), a zero-mean Gaussian prior $p(\mathbf{m}) = \mathcal{N}(-0.1 \text{ m}, 0.1 \text{ m})$ on the strike-slip component and include 5 mm of observational uncertainty in $\mathbf{C}_\mathrm{d}$. We do not account for epistemic uncertainties as our forward model is the replicate of the one used to generate the data. We first solve for the "co" and "post" slip following the CTW approach (Figures 1a and 1c). Then, we run independent inversions, one to solve for the "co" slip and the other one to infer the "co+post" slip, the post-seismic solution being the difference between "co" and "co+post" models (Figures 1b and 1d).

3.2 Results

Both independent and CTW inversion approaches allow to correctly infer the "co" slip, as the median of the PDFs is very close to the target model (Figures 1a and 1b). As expected from the inversion of surface data, the resolution is very good on shallow parts of the fault but quickly decreases with depth. The posterior uncertainty on deepest parameters is slightly decreased because the lower tip of the fault acts as an additional constrain. In contrast, the inversion methodology has a larger impact on the inferred "post" slip distributions. When jointly inverting "co" and "co+post" observations, the correct "post" slip is well estimated at almost all subfaults (Figure 1c). When solving the two slip stages separately, the mean of the models is not as good at estimating the target model (Figure 1d). The reduced posterior uncertainty of the "post" model for the independent inversion is an artifact resulting from the substraction of two gaussian-shaped curves.

In summary, the two inversion approaches allow to reliably infer the "co" slip distributions, probably because its signal is dominating in the observations. But the CTW approach provides a more robust estimation of the "post" slip distribution. In this 2D case, co-seismic and co+post signals have been observed by the same number of stations. However, for most earthquakes, the number of "co" data points available (usually GNSS) will be very limited compared to the quantity of "co+post" observations (usually InSAR). We thus expect that if performing independent inversions for a real event, the inferred "co" slip distribution will be less reliable than in the case of a CTW inversion, where the whole "co+post" dataset is used to guide the choice of co-seismic parameters. We now compare these two approaches on a real earthquake.

4 Application to the 2009 $\mathrm{M_w}$6.3 L'Aquila earthquake, Central Italy

The L'Aquila earthquake nucleated within the Apennines orogenic system (Figure 2), where the current seismic activity results from the ongoing extensional tectonics of the area. The mainshock nucleated on the Paganica fault [Figure 2, *Atzori et al.*, 2009; *Falcucci et al.*, 2009; *Chiaraluce et al.*, 2011; *Vittori et al.*, 2011; *Lavecchia et al.*, 2012; *Cheloni et al.*, 2014], southwest of the city of L'Aquila, and has been followed by at least 4 aftershocks of $\mathrm{M_w} > 5$ [*Scognamiglio et al.*, 2009; *Chiarabba et al.*, 2009; *Pondrelli et al.*, 2010]. Although the L'Aquila earthquake has been intensively studied, most co- and post-seismic models have considered the first days of post-seismic deformation as if they were part of the co-seismic phase [e.g. *Anzidei et al.*, 2009; *Atzori et al.*, 2009; *Cheloni et al.*, 2010; *Trasatti et al.*, 2011; *Cirella et al.*, 2012; *D'Agostino et al.*, 2012; *Cheloni et al.*, 2014; *Balestra and Delouis*, 2015; *Volpe et al.*, 2015]. To avoid the contamination of co-seismic signal by early afterslip, *Yano et al.* [2014] proposed to explore independently the early post-seismic deformation, yet with datasets covering different time intervals (1

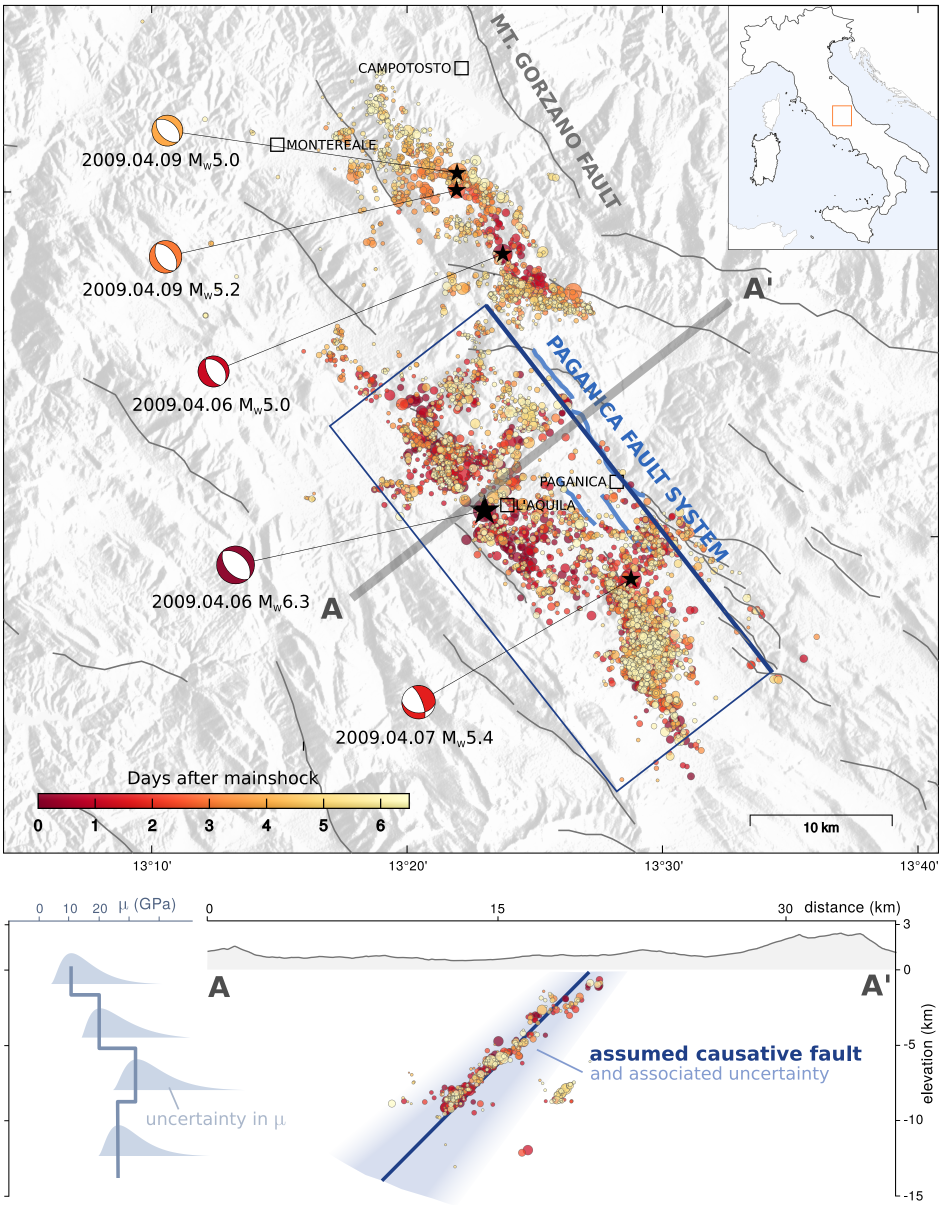

Figure 2. Seismotectonic framework of the area involved in the 2009 seismic sequence (top) and assumed forward model and associated uncertainties (bottom). In the map, couloured circles are the aftershocks from 2009 April 6 at 01:32 UTC to 2009 April 12, from the catalog of *Valoroso et al.* [2013]. The aftershocks are couloured from their occurence time after the mainshock. Beach balls are the focal mechanisms of the mainshock and four main aftershocks, with their respective epicenters located by black stars. Solid gray lines are the major seismogenic faults of the area [*Boncio et al.*, 2004a; *Lavecchia et al.*, 2012]. The observed co-seismic surface rupture is indicated with continuous blue lines [*Boncio et al.*, 2010]. Our assumed fault geometry is shown with a dark blue rectangle. In the elevation profile (bottom), uncertainty in the fault geometry is illustrated in blue. The assumed elastic modulus μ and associated uncertainties are also illustrated for the 12 first kilometers below the Earth surface.

day after the mainshock for GNSS, 6 days for InSAR). Significant post-seismic displacement is recorded up to several months after the mainshock [e.g. *D'Agostino et al.*, 2012; *Gualandi et al.*, 2014; *Cheloni et al.*, 2014; *Albano et al.*, 2015], yet most studies of long-term post-seismic signal did not analyze the first few days of post-seismic deformation.

4.1 Data, Forward Model and Prior Information

From a geodetic perspective, this event has been particularly well documented. We can distinguish two main static datasets: one which is strictly co-seismic ("co", using continuous GNSS data), and the other which also includes some days of post-seismic slip ("co+post", using cGNSS and InSAR). Two SAR images were acquired 6 days after the mainshock rupture, making the L'Aquila earthquake a perfect case study for our proposed approach. The "co" dataset corresponds to surface displacements measured between the earthquake time occurrence (t_0) and 25-30 s after t_0, and includes the static offsets of 41 (including high-rates) GPS stations surrounding the earthquake area processed by *Avallone et al.* [2011]. The "co+post" dataset covers the co-seismic phase plus 6 days of post-seismic slip, documented by 40 static GPS offsets and 2 InSAR frames: an ascending COSMO-SkyMed frame and a descending Envisat frame (Tab. S1). The observations and their processing are detailed in Supplementary Material [Section S1, *Rosen et al.*, 2004; *Lohman and Simons*, 2005; *Jolivet et al.*, 2012].

The Paganica fault is generally thought to be responsible for the co-seismic rupture of the L'Aquila earthquake, and also for most of its post-seismic deformation [*D'Agostino et al.*, 2012; *Cheloni et al.*, 2014; *Yano et al.*, 2014] along with the northernmost Campotosto fault [Figure 2, *Gualandi et al.*, 2014]. Although the distribution of relocalized aftershocks and surface rupture suggest that the Paganica fault system is possibly segmented [*Boncio et al.*, 2010; *Lavecchia et al.*, 2012] and/or curved at depth [*Chiaraluce et al.*, 2011; *Lavecchia et al.*, 2012; *Valoroso et al.*, 2013], its geometry remains poorly constrained below the surface. The variability of published morphologies for the causative fault [*Lavecchia et al.*, 2012] suggests that even with a large amount of observations and a great seismotectonic knowledge of the area, it is not possible to determine a unique fault geometry. This is why we approximate the Paganica fault geometry as a planar surface. We determine strike and position from the trace of the co-seismic surface rupture [*EMERGEO Working Group*, 2010; *Boncio et al.*, 2010] and formerly identified seismogenic faults [e.g. *Boncio et al.*, 2004b]. We select the dip and width based on aftershocks relocations and focal mechanisms [e.g. *Chiaraluce et al.*, 2011; *Chiaraluce*, 2012; *Valoroso et al.*, 2013]. Hence, our preferred geometry extends over 25 km south of coordinates (13.386° E, 42.445° N) with a strike of N142°. We set fault dip at 54° and width at 18 km, such that the fault is reaching the ground surface. This geometry is in agreement with already proposed causative structures [e.g. *Lavecchia et al.*, 2012]. The fault is divided into 154 subfaults of 1.8 km length and 1.6 km width. As our fault geometry does not reflect the reality and is poorly constrained, we account for its uncertainties [*Ragon et al.*, 2018] and assume a standard deviation on the fault dip of 5° and on the fault position of 1.5 km, regarding the discrepancies between published fault models [e.g. *Lavecchia et al.*, 2012].

We perform the static slip inversion assuming a 1-D layered elastic structure derived from the CIA velocity model [*Herrmann et al.*, 2011], and calculate Green's functions with the EDKS software [*Zhu and Rivera*, 2002]. We precompute Green's functions at depths intervals of 500 m down to 15 km depth and every 5 km below. Laterally, the Green's functions are computed every kilometer to reach the maximum epicentral distance of 100 km. Then, we interpolate and sum pre-computed Green's functions given our fault geometry and data locations. The strong variability in published elastic models for the central Italy [*Herrmann et al.*, 2011] can have a strong influence on co-seismic slip estimates [e.g. *Trasatti et al.*, 2011; *Volpe et al.*, 2012; *Gallovic et al.*, 2015]. We thus account for the uncertainties in our Earth model [*Duputel et al.*, 2014] assuming a standard deviation on shear modulus of 4 % at depths greater than 15 km and 13 % above. These values have been chosen a priori considering the variability between layered models and the horizontal variability of 3D crustal models for several depth intervals [*Magnoni et al.*, 2014].

We perform our static slip inversion as previously detailed in Section 2. We specify prior distributions for each model parameter: a zero-mean Gaussian prior $p(\mathbf{m}) = \mathcal{N}$(-10 cm, 10 cm) on the strike-slip component (we assume that, on average, the slip direction is along dip) and we consider each possible value of dip-slip displacement equally likely if it does not exceed 20 cm of reverse slip and 5 m of normal slip: $p(\mathbf{m}) = \mathcal{U}$(-20 cm, 500 cm).

4.2 Co-seismic and early post-seismic slip models

We will start by analyzing models inferred by the independent approach as applied to the two datasets. The first model is inferred from "co" data (model COgps) and the second is estimated from the "co+post" dataset (model COPOST). The "co+post" dataset is similar to what has been used in several previous studies to infer the co-seismic slip [*Cirella et al.*, 2012; *D'Agostino et al.*, 2012; *Cheloni et al.*, 2014; *Yano et al.*, 2014; *Volpe et al.*, 2015]. The results of these two inversions will then be compared to those of the CTW inversion. For the sake of comparison, these inversions are performed without accounting for epistemic uncertainties. This refinement will only be added in a final inversion.

For each approach, the results are a set of 300,000 models corresponding to the most plausible samples of the full solution space whose interpretation can provide numerous information: posterior uncertainty of the parameters, trade-off between parameters of the model, entropy of our model, etc. As we are tied to the need of presenting our results with 2D figures when the exploration is done on a parameter space of tenth of dimensions, we choose to represent our results in 3 different ways. In the main manuscript, the first representation illustrates the relations between neighboring subfaults and the variability of most probable parameters. To do so, we divide our models into 25 families, and represent the median model of each family in different pixels in each subfault (e.g. Figures 3a-d, 5a-b). A selected model will be added to the first family if it is equal to the median of the 300,000 models within a tolerance of 50 cm (for each co-seismic parameter) or 25 cm (for post-seismic parameters). The other families of models are built iteratively. If the selected model does not fall into the first family, it is used as model of reference to define the next family. When 24 families have been created, orphaned samples are added to the 25th family (more information in Figure S2). A second representation shows the posterior Probability Density Functions which, for a particular parameter, will inform on the amount of slip uncertainty associated to each subfault (e.g. Figures 3e-g, 5c-e). Our third representation shows the median models of the 300,000 inferred samples in map view (e.g. Figures a and b in S3, S5, S9).

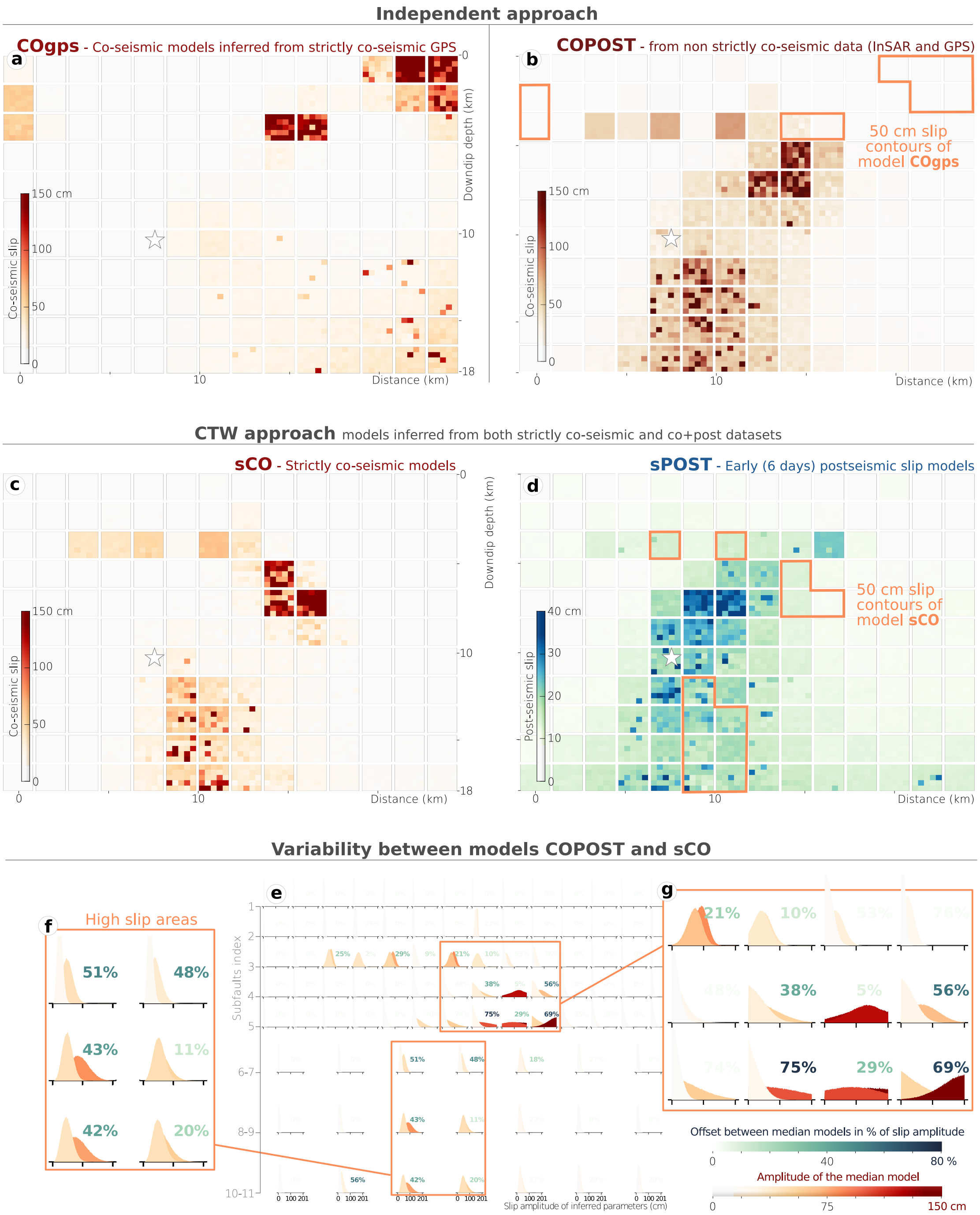

Figure 3. Comparison between finite-fault models inferred with the independent or the CTW approach. (a) Strictly co-seismic (30 s after the mainshock) slip model, named COgps, inferred from the strictly co-seismic dataset (GPS only). (b) Non-strictly co-seismic model COPOST inferred from the co-seismic dataset contaminated with some post-seismic deformation. (c) and (d) Strictly co-seismic sCO and early postseismic sPOST (6 days after the mainshock) slip models inferred jointly with the CTW approach. (a) to (d) illustrate the slip amplitude of the median models of 25 families of inferred models (more information in the text and Figure S2). Each subfault (large square) is divided into 25 pixels colored from the slip amplitude of the corresponding median model.

Figure 3. (Previous page.) (e) Comparison between the posterior Probability Density Functions of models COPOST (b) and sCO (c), colored from the amplitude of their median model. In the last four rows, the PDFs show the repartition of parameters for patches covering 2 subfaults along strike and 2 subfaults along dip (i.e. patches two times bigger than for the first four rows). The COPOST model PDFs are in the background while the sCO PDFs are in the foreground. The offset between the median models is shown as percentage with a different color scale. Two high slip areas are illustrated in detail: the highest slip patch (g) and the deep slip patch (f).

4.2.1 Approaches assuming independent datasets

When solving for the model COgps, we find that most of the slip is concentrated in the shallow parts of the fault (Figures 3a, S3a,c,e). Slip amplitudes reach 230 cm in the first two kilometers below the Earth surface. These values largely contradict field observations hardly reporting more than 15 cm of surface offset [*Falcucci et al.*, 2009; *Vittori et al.*, 2011]. This contradiction probably derives from our limited set of observations, with only 4 GPS stations documenting the rupture in the near field (Figure 4a). The COgps model is thus largely under-determined and unlikely to represent a reliable image of the co-seismic deformation. In contrast, the COPOST slip model is inferred from a more populated dataset extending over a large part of the Paganica fault (Figures 3b, S3b,d,f). The patch of highest slip amplitude, reaching more than 150 cm, is well constrained and located between 5 to 7 km depth (Figure 3b). Up to 100 cm slip is also inferred below the epicenter. The scalar seismic moment of model COPOST, calculated with $\mu = 3.5\ 10^{10}$, is $M_0 = 4.9 \pm 0.67\ 10^{25}$ dyne.m. This value corresponds to a M_w 6.4 earthquake rather than a M_w 6.3. The comparison between observations and predicted surface displacement is shown in Figure 4 for the GPS datasets and in Figure S4 for the interferograms. As expected, the COgps model well explain the "co" dataset (Figure 4b), but its predictions hardly fit the interferograms of the "co+post" dataset (Table S2). In contrast, the predicted surface displacement of the COPOST model well approaches the "co+post" observations (Figures 4b and S4), with limited residuals (Tab. S2).

4.2.2 Dual time approach, without epistemic uncertainties

With the CTW approach, we infer two slip models: the strictly co-seismic model sCO (see Figures 3c, S5a,c,e and S6 for an animated compilation of probable models) and the model sPOST which reflects the 6 days displacement following the mainshock (Figures 3d and S5b,d,f). The model sCO, exploiting information from both the "co" and "co+post" datasets, is in agreement with the main characteristics of the COPOST model (Figure 3b): the location and amplitude of the maximum slip patch are comparable, and a large amount of slip is also inferred at depth, up to 75 cm on average and exceeding 150 cm for some models (Figure 3c). However, unlike the COPOST model, the two main slip patches of the sCO model are delimited by an unruptured area (Figure 3c). Overall, the two models differ on average by 44% and by up to 75% for some subfaults characterized by high slip amplitudes (Figures 3e-g, S7), mainly because of the variability of the amount of slip inferred below 5 km depth. For the model sCO, $M_0 = 3.50 \pm 0.63\ 10^{25}$ dyne.m, corresponding to the moment magnitude value (GCMT) of 6.3.

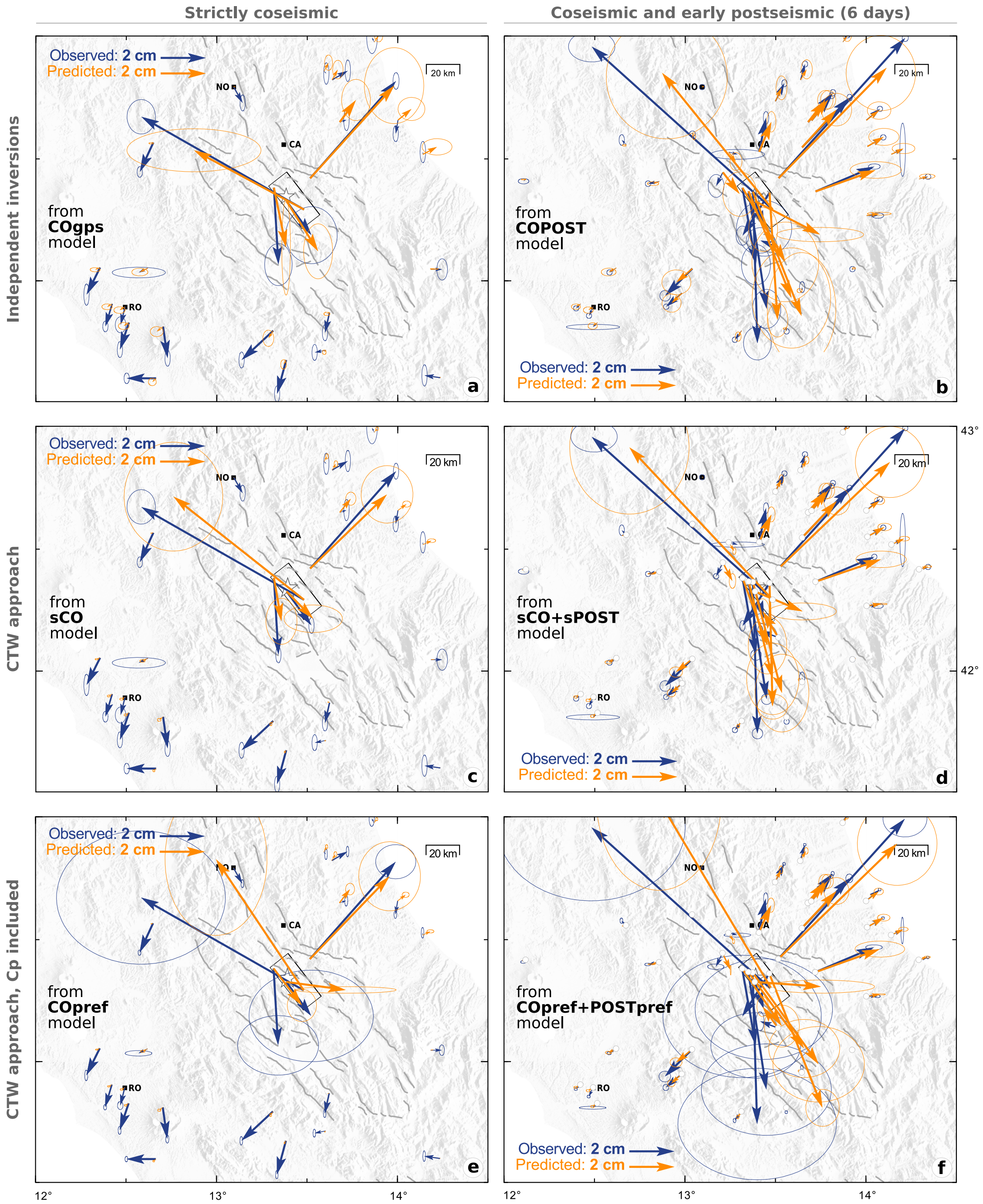

Figure 4. Comparison of horizontal surface displacement at GPS stations. Strictly co-seismic displacement is shown on the left while "co+post" displacement is shown on the right. Observed surface displacement is in blue with 95% confidence ellipses. Predictions are in orange with 95% confidence ellipses. In the top and middle rows, observational confidence ellipses (in blue) include only data errors. (a) and (b) The predictions have been calculated independently: using "co" data (a) and the "co+post" dataset (b). In (c) and (d), predictions are derived from the CTW approach. (e) and (f) show the predictions for a similar inversion setup, except epistemic uncertainties have been added to the data errors, enlarging the confidence ellipses. Our fault geometry is shown with a black rectangular box. The cities of Norcia (NO), Campotosto (CA) and Roma (RO) are indicated with black squares. Major seismogenic faults are shown in gray solid lines and the epicenter is the white star.

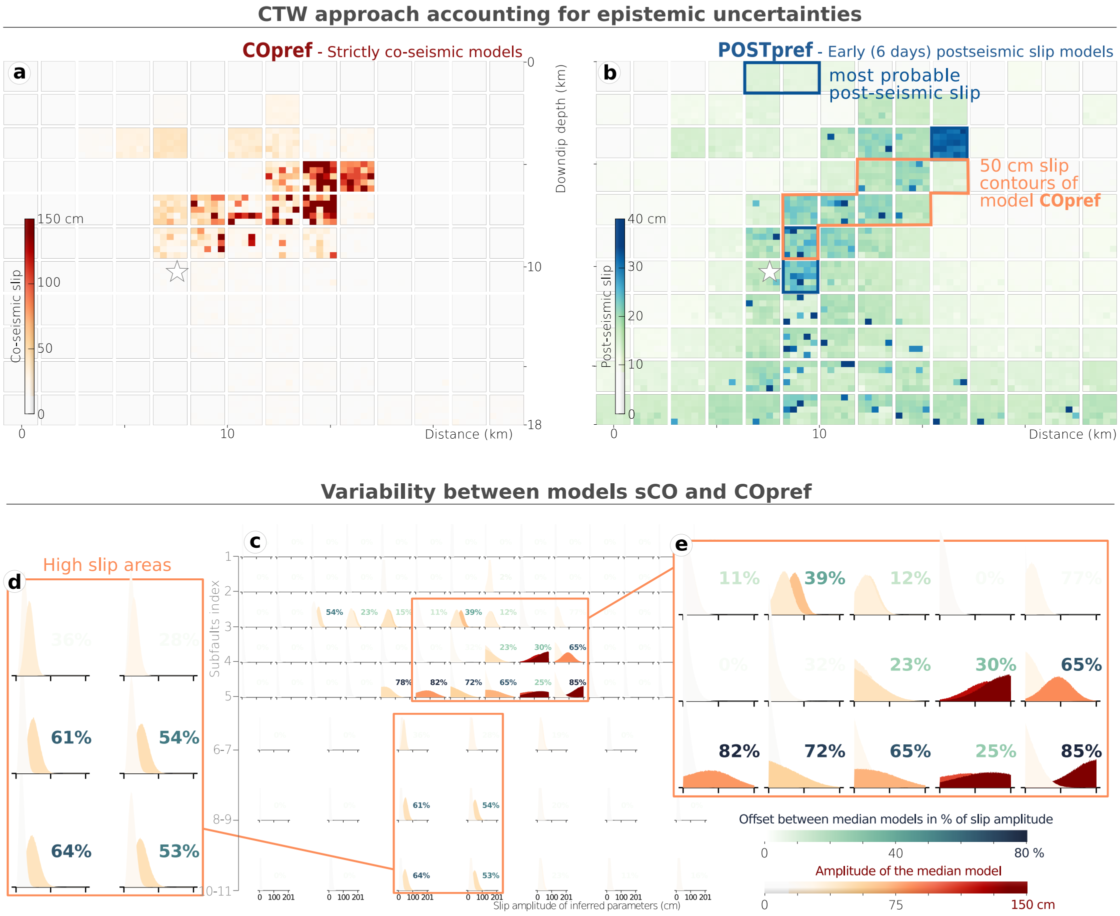

Figure 5. (a) and (b) Strictly co-seismic COpref and early postseismic POSTpref (6 days after the mainshock) preferred slip models, inferred with the CTW approach and accounting for epistemic uncertainties. (c) Comparison between the posterior Probability Density Functions of models COpref (a) and sCO (Figure 3c), colored from the amplitude of their median model. In the last four rows, the PDFs show the repartition of parameters for patches covering 2 subfaults along strike and 2 subfaults along dip (i.e. patches two times bigger than for the first four rows). The COpref model PDFs are in the foreground while the sCO PDFs are in the background. The offset between the median models is shown as percentage with a different color scale. Two high slip areas are illustrated in detail: the highest slip patch (e) and the deep slip patch (d).

With the CTW approach, we also find that a large portion of the fault slipped during a 6 days time window after the mainshock (Figure 3d), with maximum amplitude of 30 cm in the dip-slip direction (Figure S5b). The largest post-seismic slip (> 45 cm) is located between the co-seismically ruptured patches (Figure 3c), and is well constrained with only 15 cm of posterior uncertainty (Figure S5f). Overall, post-seismic slip (30 cm and below) tends to locate around the highest co-seismic slip patch and the epicenter, but also overlaps the deepest co-seismic slip patch. Yet, below 10 km depth, the posterior uncertainty can reach 100% of the median slip amplitude, meaning that it is difficult to interpret anything at that level of detail (Figures S5d,f). The seismic moment of model sPOST is $M_0 = 1.58 \pm 0.63 \; 10^{25}$ dyne.m. The predicted surface displacements fit well the observations (Figures 4c,d and Figure S8) with residuals similar to the ones of the COPOST model (Tab. S2).

As expected, the areas of largest post-seismic slip in the sPOST model correspond to the locations of largest divergence between COPOST and sCO models (3b-g). In summary, usual approaches using independent datasets do not allow us to infer reliable images of the strictly co-seismic and early post-seismic phases. Whereas the "co+post" slip model is reliable, the "co" model is not robust enough to retrieve the early afterslip from the subtraction of these two slip distributions. Additionally, the scalar seismic moment of model "co+post" corresponds to a moment magnitude greater than the GCMT M_w of 6.3. In contrast, the CTW approach allows us to infer robust estimates of both co-seismic and post-seismic slip, to exploit all the information collected within our geodetic observations, and to correctly estimate the seismic moment. However, the reliability of these models can be questioned as they do not account for uncertainties in the forward model.

4.2.3 Dual time approach, accounting for epistemic uncertainties

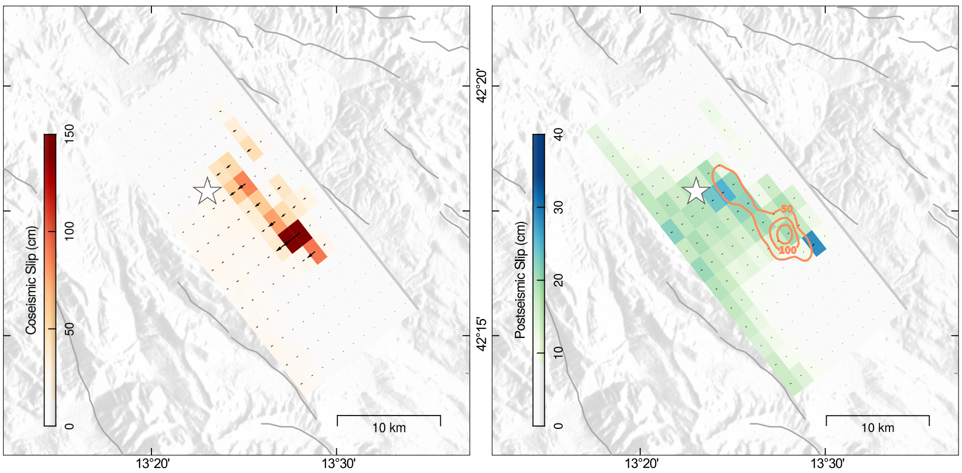

Figure 6. Our preferred slip models of the L'Aquila earthquake, inferred with the CTW approach and accounting for epistemic uncertainties. (a) and (b) show the dip-slip amplitude and rake of the average model in map view, the epicenter being the white star. In (b), orange lines also show the 50 cm co-seismic slip contours.

Here, we present the results of the CTW approach, as in the previous section, but accounting for epistemic uncertainties. We will name the resulting models COpref and POSTpref since they correspond to our preferred approach providing the most complete and objective evaluation of the problem (see Figures 5, 6, S9 and S11 for an animated compilation of probable co-seismic models). The distribution of the co-seismic slip differs by 42% on average and by up to 88% locally from the models inferred without accounting for uncertainties (Figures 5c, S10). The co-seismic slip is now limited (on average) to a single 10 km long patch located between 5 and 10 km depth, reaching more than 150 cm amplitude to the south (right-hand side of Figure 5a). The corresponding scalar seismic moment $M_0 = 3.03 \pm 0.64\ 10^{25}$ dyne.m is slightly lower than what was estimated for the model sCO but is still very close ($M_w = 6.28 \pm 0.06$) to the (GCMT) value of M_w 6.3.

Compared to the COpref model, the main characteristics of the POSTpref model are not strongly affected by the inclusion of uncertainties. Overall, post-seismic slip (20 cm and below) occurs mostly below the co-seismic high slip patch, where almost no (less than 20 cm) co-seismic slip is imaged. Subfaults with the largest post-seismic slip (more than 40 cm) tend to be located around or on the edges of the co-seismic high slip patch (Figure 5b). The presence of large post-seismic slip below 10 km depth is unlikely as the posterior uncertainty reaches 150% of the median slip (Figure S19f). Thus, only 3 narrow zones most probably slipped post-seismically (see Figure 5b, and a comparison of median and maximum a posteriori models in Figure S12). M_0 is similar to model sPOST with a value of $1.60 \pm 0.63\ 10^{25}$ dyne.m. The addition of epistemic uncertainties has increased the residuals between observations and predictions (see Tab. S2 and Figure S13). This behavior was expected as the inclusion of $\mathbf{C}_\mathrm{p}$ allows the inversion to tolerate for larger misfits at data points where the forward model predictions are less reliable [*Ragon et al.*, 2018].

In summary, the CTW approach shows that if early post-seismic is not acknowledged as post-seismic signal, co-seismic models may be biased by more than 40% on average and of up to 75% locally. But we also learn from these different tests that adding more data into the problem is not sufficient, and epistemic uncertainties remain critical for the inference of a reliable model. Altogether, our results emphasize the need to account for two types of bias in the slip models: the contamination of co-seismic observations by some early post-seismic signal, and not acknowledging for the uncertainties associated to the forward problem.

5 Discussion

5.1 Discussion of the CTW approach

Observations of co-seismic or post-seismic processes are often contaminated by other sources of deformation (mainly post-seismic or co-seismic, respectively) and are widely used, when non-contaminated data are rare and scarcely distributed. Optimizing the use of the information content in each dataset is thus critical to improve the robustness of both co-seismic and post-seismic slip models. A first approach would be to account for potential uncertainties in the co-seismic model due to early afterslip in the form of a covariance matrix, as already proposed in *Bletery et al.* [2016]. While this approach helps inferring more reliable co-seismic models at a low computational cost, it does not allow us to estimate the early afterslip and needs a prior evaluation of the amount of afterslip considered as co-seismic signal. Another strategy would be to jointly infer "co" and "co+post" data as if they were strictly co-seismic, and to select models that better explain the "co" observations, as in [*Chlieh et al.*, 2007]. In this case, the computational cost is increased because several models have to be tested. Additionally, with these approaches the early post-seismic slip is not estimated. In contrast, the CTW approach we use in this study allows us to discriminate co-seismic from early post-seismic slip and to reliably estimate corresponding slip models. Our approach takes advantage of the InSAR data that recorded both co- and post-seismic deformation to help constrain both strictly co- and early post-seismic models.

Our results on the L'Aquila event show that the early afterslip, here corresponding to 6 days after the co-seismic rupture, can reach a fourth to a third of the amplitude of the co-seismic slip. If the early afterslip is acknowledged as co-seismic signal, co-seismic

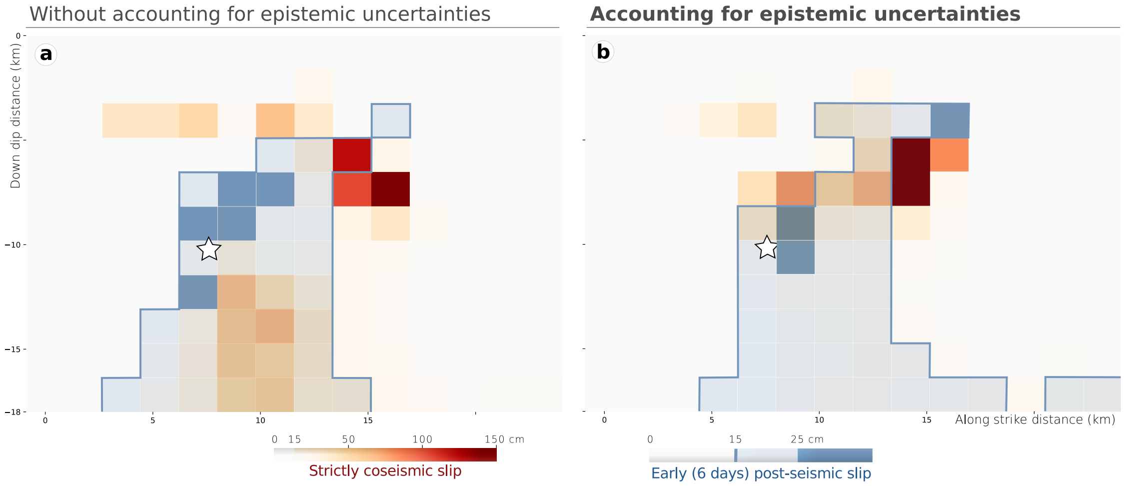

Figure 7. Effect of epistemic uncertainties ($\mathbf{C_p}$) on the distribution of strictly co-seismic slip and afterslip. The slip models have been inferred accounting for epistemic uncertainties (b) or not (a). The strictly co-seismic slip median model is in light gray to dark orange colorscale. The subfaults that slipped of more than 15 to 25 cm up to 6 days after the mainshock, according to our median model, are in transparent light to medium blue. The afterslip does not overlap the co-seismic slip when $\mathbf{C_p}$ is accounted for (b), whereas the two slip distributions overlap at depth when no $\mathbf{C_p}$ is included (a).

models of the l'Aquila event are biased. The impact of early afterslip on the co-seismic models is particularly large in the case of the L'Aquila event and questions the generic nature of this result. Overall, early afterslip remains poorly studied but has been shown to range from 0.6% to more than 8% of the co-seismic peak slip in the first 3-4 hours following an earthquake [respectively for the 2009 great Tohoku-Oki earthquake and the 2012 M_w7.6 Nicoya earthquake, *Munekane*, 2012; *Malservisi et al.*, 2015]. Thus, that the post-seismic deformation ongoing 6 days after the mainshock reaches up to 20 % of the co-seismic slip of the L'Aquila earthquake might not be an extreme case.

Our tests also demonstrate that models are largely impacted by the introduction of epistemic uncertainties (Figure 7). This impact could mean the assumed fault and Earth properties are not realistic enough to capture the real seismic rupture, and/or that small variations of the fault geometry (slight curvature, roughness) or of the Earth model (3D heterogeneities) largely affect our slip models. The influence of epistemic uncertainties is greater on the co-seismic model, as expected from the fact that these uncertainties scale with the amount of slip [*Duputel et al.*, 2014; *Ragon et al.*, 2018]. Accounting for uncertainties of the forward model allowed us to exclude the possibility of deep slip for the co-seismic models, but not totally for the post-seismic models probably because of the much lower slip amplitudes. Additionally, accounting for $\mathbf{C_p}$ prevented the most probable co- and post-seismic slips to overlap in deeper parts of the fault. The inclusion of epistemic uncertainties acts like a smoothing constraint on the slip distribution, but with a smoothing factor being controlled by the inaccuracies of the forward problem.

5.2 Non-unicity of co-seismic and afterslip models of the L'Aquila earthquake

Our results on the L'Aquila event indicate that the strictly co-seismic slip is concentrated in a thin horizontal band located between 5 and 7 km depth and reaching more than 150 cm in amplitude at its southern end, with no large slip amplitudes inferred below 8 km depth (Figures 6 and 8). The highest amplitude is reached at about 6 km depth south west of the epicenter, a rupture area also imaged in the co-seismic models of *Gua-*

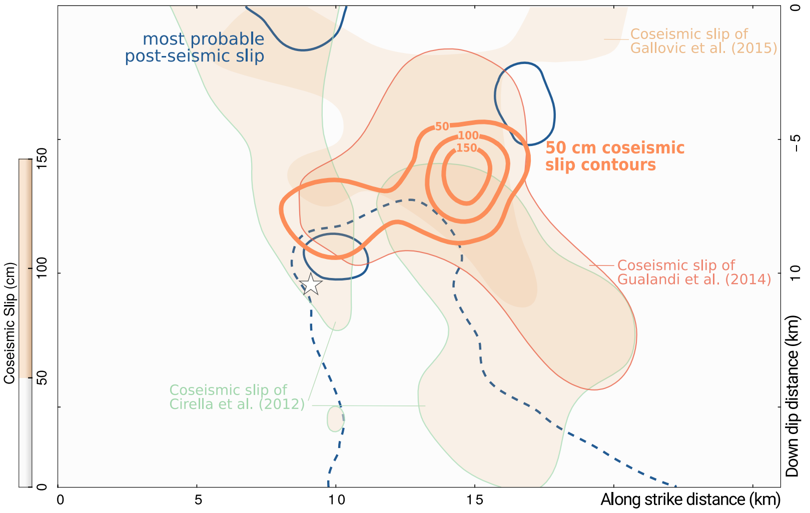

Figure 8. Comparison between the slip distributions inferred with the CTW approach and co-seismic slip distributions of other studies. The strictly co-seismic slip of *Gualandi et al.* [2014] inferred from GPS only, the strictly co-seismic slip of *Gallovic et al.* [2015] inferred from accelerometric and high rate GPS data, the co-seismic slip of *Cirella et al.* [2012] inferred from GPS, InSAR and strong motion, are projected in our fault plane in transparent light orange when slip exceeds 50 cm. The 50 cm contours of our strictly co-seismic slip distribution and the 15 cm contours of our afterslip inferred accounting for epistemic uncertainties are in bold lines, respectively orange and dark blue. The epicenter is the white star.

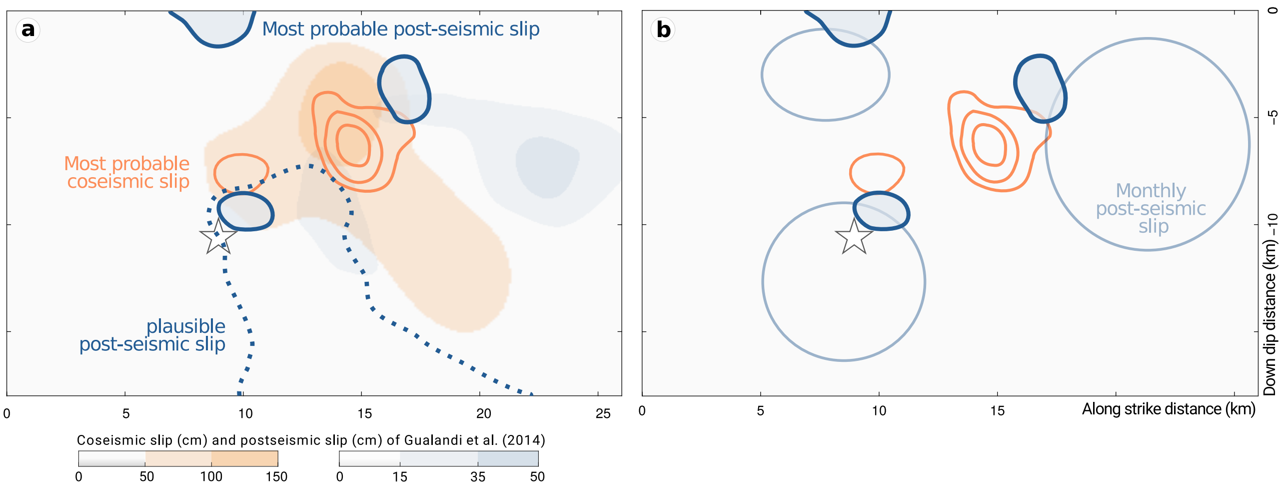

Figure 9. Comparison between our most probable strictly co- and post-seismic slip distribution 6 days after the mainshock and the post-seismic slip up to 306 days after the mainshock. (a) Our most probable slip distributions are represented with bold orange and dark blue lines, respectively for co-seismic (50 cm contours) and post-seismic slip (slip >10 cm). The area of afterslip delimited with a dotted blue line is considered as less plausible as inferred with large uncertainties. The co-seismic slip and afterslip 306 days after the mainshock inferred by *Gualandi et al.* [2014] are plotted with the same color codes but as color swaths. (b) Our results are compared to the area that slipped post-seismically during about 6 months (176 and 194 days respectively) after the mainshock as modeled by *D'Agostino et al.* [2012] and *Cheloni et al.* [2014]. The epicenter is the white star.

landi et al. [2014], *Gallovic et al.* [2015] and *Cirella et al.* [2012] (inferred respectively from GPS only, from accelerometric and high rate GPS data, and from GPS, InSAR and strong motion, see Figure 8) and most of other authors [*Atzori et al.*, 2009; *Trasatti et al.*, 2011; *D'Agostino et al.*, 2012; *Serpelloni et al.*, 2012; *Cheloni et al.*, 2014; *Balestra and Delouis*, 2015; *Volpe et al.*, 2015]. It is the only recurrent pattern we can notice between the 4 slip models of Figure 8. Indeed, while we do not image any shallow slip, other published slip models do with up to 1.5 m in amplitude [Figure 8, *Cirella et al.*, 2012; *Volpe et al.*, 2015]. At greater depths, most authors infer large slip amplitudes while our preferred model shows no slip below 8 km depth.

The imaged patches of post-seismic slip (>15 cm) are located around our co-seismic slip, near its epicenter and southern end. Interestingly, our inferred post-seismic slip is also located near areas that ruptured co-seismically as inferred by other studies (Figure 8). The post-seismic slip that occurred several days to months after the mainshock is characterized by 3 wide slip areas, located SW of the main co-seismic slip patch, above the epicenter close to the surface, and around the epicenter [*D'Agostino et al.*, 2012; *Cheloni et al.*, 2014; *Gualandi et al.*, 2014]. Most of these post-seismic models acknowledge the first days of post-seismic signal as a co-seismic deformation. While we infer likely afterslip in similar locations, the afterslip patches are limited to narrower areas near the co-seismic rupture (Figure 9). Most of these longer-term post-seismic models cover time periods ranging from 6 days to 9 months after the mainshock, they overlook a large part of the early post-seismic deformation. Thus, the peak amplitude of the early afterslip is up to 3 times larger than what was imaged for several months by *D'Agostino et al.* [2012] and *Cheloni et al.* [2014].

Our results show that the amplitude and distribution of long-term afterslip may be largely underestimated (here by a factor of 3) if the deformation occurring the first few hours to days after the mainshock is not accounted in the post-seismic budget. Thus, overlooking the early part of the postseismic phase measured in geodetic data may not only bias the estimates of the coseismic slip, but also our estimates of the postseismic phase.

5.3 Fault frictional properties and relationship between afterslip and aftershocks

The comparison between our early post-seismic model and images of longer-term post-seismic slip suggest that afterslip may nucleate preferably around the co-seismic rupture in the days following the mainshock (Figure 9b). Afterwards, the afterslip propagates and extends, both along-dip and laterally, away from the co-seismic slip [*D'Agostino et al.*, 2012; *Cheloni et al.*, 2014; *Gualandi et al.*, 2014]. This behavior agrees with models explaining afterslip as a result of rate dependent friction behavior. Indeed, in these models the afterslip relaxes the stress increment induced in velocity-strengthening area by the co-seismic rupture [*Marone et al.*, 1991; *Perfettini and Avouac*, 2004]. The post-seismic sliding thus nucleates close to the mainshock asperity and propagates with time outward from the rupture zone. That early afterslip relates to the stress changes induced by the co-seismic rupture has also been modeled for other events [e.g. the M_w8.0 Tokachi-oki, M_w7.6 Chi-Chi, and the M_w6.0 Parkfield, *Miyazaki et al.*, 2004; *Chan and Stein*, 2009; *Wang et al.*, 2012, respectively].

Additionally, our results show that early afterslip nucleate within narrow areas (1-2 km wide), and does not happen everywhere around the co-seismic rupture. Areas sliding aseismically just after the mainshock are thus limited in size around the co-seismic rupture, suggesting that frictional properties vary at a small-scale around the rupture zone. It may also suggest that the regions adjacent to co-seismic rupture are potentially unstable (i.e. are steady-state velocity weakening) . This interpretation agrees with the results of *Gualandi et al.* [2014] suggesting the longer-term afterslip regions, that are also located farther away from the co-seismic ruptured zone, are characterized by a transition between velocity weakening and velocity strengthening behavior. This implies that co-seismic rupture occurs and triggers early afterslip in velocity weakening regions; while afterslip propagates away from the ruptured zone in fault regions that progressively become stable with the distance to the mainshock.

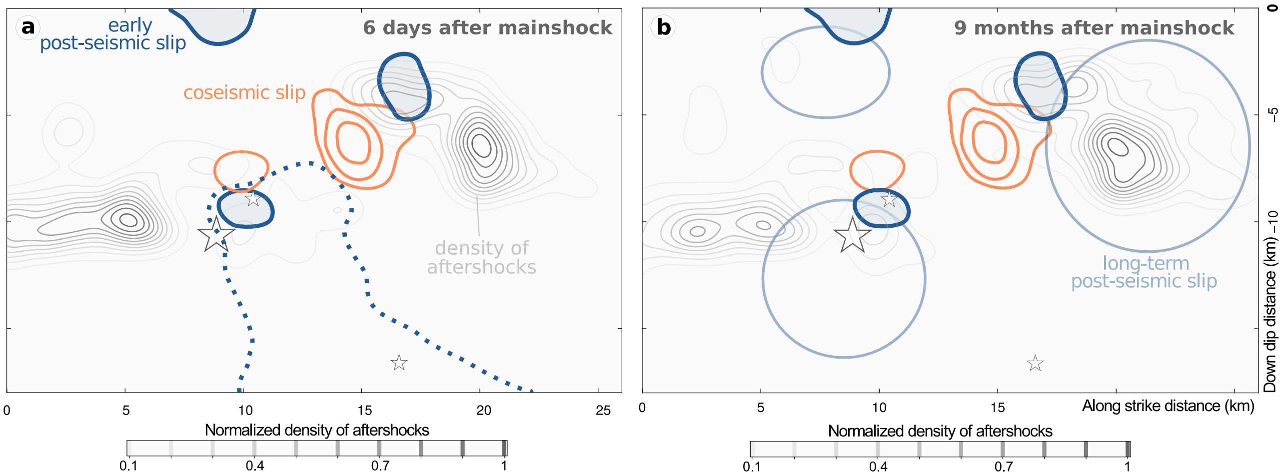

Figure 10. Distribution of most probable co-seismic slip and afterslip models, and the normalized density of aftershocks that occurred (a) within 6 days after the mainshock or (b) up to 9 months after the mainshock [$M_C = 0.88$, catalog of *Valoroso et al.*, 2013]. The strictly co-seismic 50 cm slip contours are in orange, while the contours of most probable afterslip (slip > 10 cm) are in blue. The area delimited by dotted blue lines has plausibly hosted some afterslip, but not as probably as the other regions. The areas that slipped post-seismically during about 6 months after the mainshock as modeled by *D'Agostino et al.* [2012], *Cheloni et al.* [2014] and *Gualandi et al.* [2014] are the blue circles. The density of aftershocks located within 3 km of the fault (to account for potential uncertainty of the fault geometry) is calculated with a kernel density estimation method [*Parzen*, 1962] with a smoothing factor of 0.6. The cumulated number of aftershocks of $M_c = 0.88$ is of ~6000 6 days after the mainshock and 8 times larger 9 months after the mainshock (Figure S14). The epicenter and aftershocks of $M_w \geq 4.4$ are the white stars.

In Figure 10, we compare the slip distributions imaged for the mainshock and 6 days after, with the distribution of aftershocks detected over 6 days and 9 months after the mainshock [*Valoroso et al.*, 2013]. As for many earthquakes, aftershocks are distributed mainly at the ends of the fault [*Das and Henry*, 2003] with few events located near the co-seismic rupture. Six days after the mainshock (Figure 10a), our results show no clear correlation between the location of early afterslip and aftershocks. Months after the mainshock, the areas with a high density of aftershocks are similar to 6 days after the mainshock [as suggested by *Henry and Das*, 2001, whereas the cumulated number of aftershocks is 8 times larger, see Figure S14] and the post-seismic slip has extended farther away from the co-seismic rupture. This is why we can observe a spatial correlation between some areas of long-term post-seismic slip and aftershocks [*D'Agostino et al.*, 2012; *Cheloni et al.*, 2014]. The spatial correlation is particularly striking for the southern afterslip patch, for which few early aftershocks are located within the early afterslip area (Figure 10a) while the aftershock cluster overlies the monthly afterslip that propagated outward from the co-seismically ruptured zone (Figure 10b).

From our results, we can thus draw only one conclusion: there is no correlation between the area of large (>15 cm) early afterslip and the location of aftershocks for the first few days after the mainshock. This conclusion contradicts the observations made for some other earthquakes although mainly at longer time scales [e.g. *Hsu et al.*, 2006; *Perfettini and Avouac*, 2007; *Wang et al.*, 2012; *Ross et al.*, 2017, for time periods spanning respectively 11 months, 3.5 years, 5 days and 2.5 months]. Our results could also suggest that, for some parts of the fault, aftershocks nucleation precedes aseismic slip that occur months after the mainshock; aftershocks could thus be partly explained by stress changes due to the co-seismic rupture. But these aftershocks could also be triggered by early afterslip with an amplitude so low that it is not inferred by our model. The absence of clear correlation between early afterslip and aftershocks may also be related to the presence of high pressure fluids in the seismogenic zone of the L'Aquila event, and of Central Italy in general, with the widespread emissions of CO_2 rich fluids for deep origin [*Chiodini et al.*, 2000; *Frezzotti et al.*, 2009; *Chiodini et al.*, 2011]. Already, *Miller et al.* [2004] and *Antonioli et al.* [2005] proposed that the aftershocks and spatio-temporal migration of the seismicity of the 1997 Umbria-Marche seismic sequence (80 km NE of the L'Aquila event) were driven by the co-seismically induced fluid pressure migration. Similarly, the increase in seismicity rate of the L'Aquila earthquake and the occurrence of some aftershocks may have been driven by fluid flows [*Luccio et al.*, 2010; *Terakawa et al.*, 2010; *Malagnini et al.*, 2012]. High pressure fluids have been observed before the co-seismic rupture, and may have impacted the nucleation phase of the L'Aquila earthquake [*Lucente et al.*, 2010]. Finally, *Malagnini et al.* [2012] show that the strength of the Campotosto fault, just north of the main rupture (see Figure 2), has been controlled by fluid migration for at least 6 days after the mainshock, a time window corresponding to our study of early afterslip. The perturbations in pore fluid pressure induced by the co-seismic rupture may have triggered the first aftershocks of the L'Aquila earthquake. Fluid migration may have prevented aftershocks and early afterslip to affect the same areas of the fault, especially if the increase in fluid pressure first produced aseismic slip, followed by triggered seismicity around the pore pressure front [*Miller et al.*, 2004]. Finally, if early aftershocks were triggered by changes in fluid pressure, it may justify the possibility that some of these early aftershocks nucleated before the occurrence of long-term afterslip in similar regions of the fault.

6 Conclusion

In this study, we use a simple and efficient approach to account for the differences in temporal resolution of various geodetic datasets. A redesign of the Green's Functions matrix allows us to optimize the use of the information content of datasets covering different time periods. With this approach, we image simultaneously the strictly co-seismic slip and the early afterslip (6 days after the mainshock) of the 2009 M_w6.3 L'Aquila earthquake using two datasets: one covers the two slip episodes (e.g. InSAR) while the other records the co-seismic signal only (e.g. continuous GNSS). We show that when the two phases are inverted independently, as is usually the case, the estimated slip distributions are not reliable because strictly co-seismic observations are usually of poor spatial resolution. Additionally, overlooking the early post-seismic deformation results in models that overestimates the co-seismic slip, and underestimates the total post-seismic slip budget. In contrast, our approach allows us to accurately estimate both co-seismic and early post-seismic slip models.

Our results show that neglecting the contribution of the early post-seismic deformation will likely bias estimates of the co-seismic and/or the post-seismic slip. For our test case of the L'Aquila earthquake, the peak co-seismic slip is likely 30% greater when early post-seismic signal is recorded as co-seismic deformation. The long-term afterslip estimates are underestimated by a factor 3 when the first 6 days of post-seismic deformation are not acknowledged. Our investigation of the L'Aquila event also stressed the strong influence of uncertainties in the forward model, mainly stemming from our imperfect knowledge of the fault geometry and the Earth structure, on the imaged slip distributions. These uncertainties alone are sufficient to cause contradictory interpretations on the slip history on the fault (e.g. with the existence of shallow or dip slip).

Our preferred slip model for the L'Aquila earthquake tends to be simpler than many previous models, with one thin horizontal band of slip located around 7km depth, reaching 150cm in amplitude near its southern end. Our model thus excludes the possibility of major shallow or deep co-seismic slip patches (less than a few km or deeper than 10). The early post-seismic slip (6 days after the mainshock) was limited to the same intermediate depth range (7 km +/- 3 km), initiating on the edges of the co-seismic slip, with possibly some overlap. Some afterslip may also have occurred at greater depths. A comparison with longer term afterslip models suggest that the early afterslip patches might have simply expanded over time from their initial position. Aftershocks are more spatially distributed (7 km +/- 5 km) but still concentrated at intermediate depth. Several studies suggest that aftershocks might be driven by afterslip [e.g., *Perfettini and Avouac*, 2007; *Hsu et al.*, 2006; *Sladen et al.*, 2010; *Ross et al.*, 2017; *Perfettini et al.*, 2018] but here aftershocks are only partially overlapping. This result suggests that post-seismic reloading may be influenced by fluids as advocated in several previous studies [e.g., *Luccio et al.*, 2010; *Terakawa et al.*, 2010; *Malagnini et al.*, 2012; *Guglielmi et al.*, 2015; *Scuderi and Collettini*, 2016].

Acknowledgments

We thank Bertrand Delouis and Frederic Cappa for helpful discussions. We are extremely grateful to Frederica Magnoni who shared her 3D crustal model for the L'Aquila area [*Magnoni et al.*, 2014], to Luisa Valoroso who provided the aftershock catalog for the L'Aquila earthquake [*Valoroso et al.*, 2013] and to Simone Atzori for sharing the InSAR data [*Atzori et al.*, 2009]. The Bayesian simulations were performed on the HPC-Regional Center ROMEO (https://romeo.univ-reims.fr) of the University of Reims Champagne-Ardenne (France). The Classic Slip Inversion (CSI) Python library created by Romain Jolivet was used to build inputs for the Bayesian algorithm. Discussed slip models of *Gualandi et al.* [2014], *Gallovic et al.* [2015] and *Cirella et al.* [2012] have been retrieved from SRCMOD [http://equake-rc.info/SRCMOD/, *Mai and Thingbaijam*, 2014]. Figures were generated with the Matplotlib and Seaborn Python libraries and with the Generic Mapping Tools library. This study was partly supported by the French National Research Agency (ANR) EPOST project ANR-14-CE03-0002. Théa Ragon is supported by a fellowship from the French Ministry of Research and Higher Education.

References

Albano, M., S. Barba, M. Saroli, M. Moro, F. Malvarosa, M. Costantini, C. Bignami, and S. Stramondo (2015), Gravity-driven postseismic deformation following the Mw 6.3 2009 L'Aquila (Italy) earthquake, *Scientific Reports*, *5*, doi:10.1038/srep16558.

Antonioli, A., D. Piccinini, L. Chiaraluce, and M. Cocco (2005), Fluid flow and seismicity pattern: Evidence from the 1997 Umbria-Marche (central Italy) seismic sequence, *Geophysical Research Letters*, *32*(10), doi:10.1029/2004GL022256.

Anzidei, M., E. Boschi, V. Cannelli, R. Devoti, A. Esposito, A. Galvani, D. Melini, G. Pietrantonio, F. Riguzzi, V. Sepe, and E. Serpelloni (2009), Coseismic deformation of the destructive April 6, 2009 L'Aquila earthquake (central Italy) from GPS data, *Geophysical Research Letters*, *36*(17), L17,307, doi:10.1029/2009GL039145.

Atzori, S., I. Hunstad, M. Chini, S. Salvi, C. Tolomei, C. Bignami, S. Stramondo, E. Trasatti, A. Antonioli, and E. Boschi (2009), Finite fault inversion of DInSAR coseismic displacement of the 2009 L'Aquila earthquake (central Italy), *Geophysical Research Letters*, *36*(15), L15,305, doi:10.1029/2009GL039293.

Avallone, A., M. Marzario, A. Cirella, A. Piatanesi, A. Rovelli, C. Di Alessandro, E. D'Anastasio, N. D'Agostino, R. Giuliani, and M. Mattone (2011), Very high rate (10 Hz) GPS seismology for moderate-magnitude earthquakes: The case of the Mw 6.3 L'Aquila (central Italy) event, *Journal of Geophysical Research: Solid Earth*, *116*(B2), B02,305, doi:10.1029/2010JB007834.

Balestra, J., and B. Delouis (2015), Reassessing the Rupture Process of the 2009 L'Aquila Earthquake (Mw 6.3) on the Paganica Fault and Investigating the Possibility of Co-seismic Motion on Secondary Faults, *Bulletin of the Seismological Society of America*, *105*(3), 1517–1539, doi:10.1785/0120140239.

Barbot, S., and Y. Fialko (2010), A unified continuum representation of post-seismic relaxation mechanisms: semi-analytic models of afterslip, poroelastic rebound and viscoelastic flow, *Geophysical Journal International*, *182*(3), 1124–1140, doi:10.1111/j.1365-246X.2010.04678.x.

Barnhart, W. D., C. M. J. Brengman, S. Li, and K. E. Peterson (2018), Ramp-flat basement structures of the Zagros Mountains inferred from co-seismic slip and afterslip of the 2017 Mw7.3 Darbandikhan, Iran/Iraq earthquake, *Earth and Planetary Science Letters*, *496*, 96–107, doi:10.1016/j.epsl.2018.05.036.

Bletery, Q., A. Sladen, J. Jiang, and M. Simons (2016), A Bayesian source model for the 2004 great Sumatra-Andaman earthquake, *Journal of Geophysical Research: Solid Earth*, p. 2016JB012911, doi:10.1002/2016JB012911.

Boncio, P., G. Lavecchia, G. Milana, and B. Rozzi (2004a), Seismogenesis in Central Apennines, Italy: an integrated analysis of minor earthquake sequences and structural data in the Amatrice-Campotosto area, *Annals of Geophysics*, *47*(6), 1723–1742.

Boncio, P., G. Lavecchia, and B. Pace (2004b), Defining a model of 3d seismogenic sources for Seismic Hazard Assessment applications: The case of central Apennines (Italy), *Journal of Seismology*, *8*(3), 407–425, doi:10.1023/B:JOSE.0000038449.78801.05.

Boncio, P., A. Pizzi, F. Brozzetti, G. Pomposo, G. Lavecchia, D. Di Naccio, and F. Ferrarini (2010), Coseismic ground deformation of the 6 April 2009 L'Aquila earthquake (central Italy, Mw6.3), *Geophysical Research Letters*, *37*(6), L06,308, doi:10.1029/2010GL042807.

Burgmann, R., P. Segall, M. Lisowski, and J. Svarc (1997), Postseismic strain following the 1989 Loma Prieta earthquake from GPS and leveling measurements, *Journal of Geophysical Research: Solid Earth*, *102*(B3), 4933–4955, doi:10.1029/96JB03171.

Chan, C.-H., and R. S. Stein (2009), Stress evolution following the 1999 Chi-Chi, Taiwan, earthquake: Consequences for afterslip, relaxation, aftershocks and departures from Omori decay, *Geophysical Journal International*, *177*(1), 179–192, doi:10.1111/j.1365-246X.2008.04069.x.

Cheloni, D., N. D'Agostino, E. D'Anastasio, A. Avallone, S. Mantenuto, R. Giuliani, M. Mattone, S. Calcaterra, P. Gambino, D. Dominici, F. Radicioni, and G. Fastellini (2010), Coseismic and initial post-seismic slip of the 2009 Mw 6.3 L'Aquila earthquake, Italy, from GPS measurements, *Geophysical Journal International*, *181*(3), 1539–1546, doi:10.1111/j.1365-246X.2010.04584.x.

Cheloni, D., R. Giuliani, E. D'Anastasio, S. Atzori, R. J. Walters, L. Bonci, N. D'Agostino, M. Mattone, S. Calcaterra, P. Gambino, F. Deninno, R. Maseroli, and G. Stefanelli (2014), Coseismic and post-seismic slip of the 2009 L'Aquila (central Italy) MW 6.3 earthquake and implications for seismic potential along the Campotosto fault from joint inversion of high-precision levelling, InSAR and GPS data, *Tectonophysics*, *622*, 168–185, doi:10.1016/j.tecto.2014.03.009.

Chiarabba, C., A. Amato, M. Anselmi, P. Baccheschi, I. Bianchi, M. Cattaneo, G. Cecere, L. Chiaraluce, M. G. Ciaccio, P. De Gori, G. De Luca, M. Di Bona, R. Di Stefano, L. Faenza, A. Govoni, L. Improta, F. P. Lucente, A. Marchetti, L. Margheriti, F. Mele, A. Michelini, G. Monachesi, M. Moretti, M. Pastori, N. Piana Agostinetti, D. Piccinini, P. Roselli, D. Seccia, and L. Valoroso (2009), The 2009 L'Aquila (central Italy) MW6.3 earthquake: Main shock and aftershocks, *Geophysical Research Letters*, *36*(18), L18,308, doi:10.1029/2009GL039627.

Chiaraluce, L. (2012), Unravelling the complexity of Apenninic extensional fault systems: A review of the 2009 L'Aquila earthquake (Central Apennines, Italy), *Journal of Structural Geology*, *42*, 2–18, doi:10.1016/j.jsg.2012.06.007.

Chiaraluce, L., L. Valoroso, D. Piccinini, R. Di Stefano, and P. De Gori (2011), The anatomy of the 2009 L'Aquila normal fault system (central Italy) imaged by high resolution foreshock and aftershock locations, *Journal of Geophysical Research: Solid Earth*, *116*(B12), B12,311, doi:10.1029/2011JB008352.

Chiodini, G., F. Frondini, C. Cardellini, F. Parello, and L. Peruzzi (2000), Rate of diffuse carbon dioxide Earth degassing estimated from carbon balance of regional aquifers: The case of central Apennine, Italy, *Journal of Geophysical Research: Solid Earth*, *105*(B4), 8423–8434, doi:10.1029/1999JB900355.

Chiodini, G., S. Caliro, C. Cardellini, F. Frondini, S. Inguaggiato, and F. Matteucci (2011), Geochemical evidence for and characterization of CO2 rich gas sources in the epicentral area of the Abruzzo 2009 earthquakes, *Earth and Planetary Science Letters*, *304*(3), 389–398, doi:10.1016/j.epsl.2011.02.016.

Chlieh, M., J.-P. Avouac, V. Hjorleifsdottir, T.-R. A. Song, C. Ji, K. Sieh, A. Sladen, H. Hebert, L. Prawirodirdjo, Y. Bock, and J. Galetzka (2007), Coseismic Slip and Afterslip of the Great Mw 9.15 SumatraâĂŞAndaman Earthquake of 2004, *Bulletin of the Seismological Society of America*, *97*(1A), S152–S173, doi:10.1785/0120050631.

Cirella, A., A. Piatanesi, E. Tinti, M. Chini, and M. Cocco (2012), Complexity of the rupture process during the 2009 L'Aquila, Italy, earthquake, *Geophysical Journal International*, *190*(1), 607–621, doi:10.1111/j.1365-246X.2012.05505.x.

Cubas, N., N. Lapusta, J.-P. Avouac, and H. Perfettini (2015), Numerical modeling of long-term earthquake sequences on the NE Japan megathrust: Comparison with observations and implications for fault friction, *Earth and Planetary Science Letters*, *419*(Supplement C), 187–198, doi:10.1016/j.epsl.2015.03.002.

D'Agostino, N., D. Cheloni, G. Fornaro, R. Giuliani, and D. Reale (2012), Space-time distribution of afterslip following the 2009 L'Aquila earthquake, *Journal of Geophysical Research: Solid Earth*, *117*(B2), B02,402, doi:10.1029/2011JB008523.

Das, S., and C. Henry (2003), Spatial relation between main earthquake slip and its aftershock distribution, *Reviews of Geophysics*, *41*(3), doi:10.1029/2002RG000119.

Delouis, B., D. Giardini, P. Lundgren, and J. Salichon (2002), Joint Inversion of InSAR, GPS, Teleseismic, and Strong-Motion Data for the Spatial and Temporal Distribution of Earthquake Slip: Application to the 1999 izmit Mainshock, *Bulletin of the Seismological Society of America*, *92*(1), 278–299, doi:10.1785/0120000806.

Dieterich, J. (1994), A constitutive law for rate of earthquake production and its application to earthquake clustering, *Journal of Geophysical Research: Solid Earth*, *99*(B2), 2601–2618, doi:10.1029/93JB02581.

Duputel, Z., P. S. Agram, M. Simons, S. E. Minson, and J. L. Beck (2014), Accounting for prediction uncertainty when inferring subsurface fault slip, *Geophysical journal international*, *197*(1), 464–482.

Elliott, J. R., A. C. Copley, R. Holley, K. Scharer, and B. Parsons (2013), The 2011 Mw 7.1 Van (Eastern Turkey) earthquake, *Journal of Geophysical Research: Solid Earth*, *118*(4), 1619–1637, doi:10.1002/jgrb.50117.

EMERGEO Working Group (2010), Evidence for surface rupture associated with the Mw 6.3 L'Aquila earthquake sequence of April 2009 (central Italy), *Terra Nova*, *22*(1), 43–51, doi:10.1111/j.1365-3121.2009.00915.x.

Falcucci, E., S. Gori, E. Peronace, G. Fubelli, M. Moro, M. Saroli, B. Giaccio, P. Messina, G. Naso, G. Scardia, A. Sposato, M. Voltaggio, P. Galli, and F. Galadini (2009), The Paganica Fault and Surface Coseismic Ruptures Caused by the 6 April 2009 Earthquake (L'Aquila, Central Italy), *Seismological Research Letters*, *80*(6), 940–950, doi:10.1785/gssrl.80.6.940.

Freed, A. M. (2007), Afterslip (and only afterslip) following the 2004 Parkfield, California, earthquake, *Geophysical Research Letters*, *34*(6), L06,312, doi:10.1029/2006GL029155.

Freed, A. M., and R. Burgmann (2004), Evidence of power-law flow in the Mojave desert mantle, *Nature*, *430*(6999), 548–51.

Frezzotti, M. L., A. Peccerillo, and G. Panza (2009), Carbonate metasomatism and CO2 lithosphereâĂŞasthenosphere degassing beneath the Western Mediterranean: An integrated model arising from petrological and geophysical data, *Chemical Geology*, *262*(1), 108–120, doi:10.1016/j.chemgeo.2009.02.015.

Gallovic, F., W. Imperatori, and P. M. Mai (2015), Effects of three-dimensional crustal structure and smoothing constraint on earthquake slip inversions: Case study of the Mw6.3 2009 L'Aquila earthquake, *Journal of Geophysical Research: Solid Earth*, *120*(1), 2014JB011,650, doi:10.1002/2014JB011650.

Gualandi, A., E. Serpelloni, and M. E. Belardinelli (2014), Space-time evolution of crustal deformation related to the Mw 6.3, 2009 L'Aquila earthquake (central Italy) from principal component analysis inversion of GPS position time-series, *Geophysical Journal International*, p. ggt522, doi:10.1093/gji/ggt522.

Gualandi, A., J.-P. Avouac, J. Galetzka, J. F. Genrich, G. Blewitt, L. B. Adhikari, B. P. Koirala, R. Gupta, B. N. Upreti, B. Pratt-Sitaula, and J. Liu-Zeng (2017), Pre- and post-seismic deformation related to the 2015, Mw7.8 Gorkha earthquake, Nepal, *Tectonophysics*, *714*(Supplement C), 90–106, doi:10.1016/j.tecto.2016.06.014.

Guglielmi, Y., F. Cappa, J.-P. Avouac, P. Henry, and D. Elsworth (2015), Seismicity triggered by fluid injectionâĂŞinduced aseismic slip, *Science*, *348*(6240), 1224–1226, doi: 10.1126/science.aab0476.

He, P., E. A. Hetland, Q. Wang, K. Ding, Y. Wen, and R. Zou (2017), Coseismic Slip in the 2016 Mw 7.8 Ecuador Earthquake Imaged from Sentinel-1a Radar Interferometry, *Seismological Research Letters*, *88*(2A), 277–286, doi:10.1785/0220160151.

Helmstetter, A., and B. E. Shaw (2009), Afterslip and aftershocks in the rate-and-state friction law, *Journal of Geophysical Research: Solid Earth*, *114*(B1), doi:10.1029/2007JB005077.

Henry, C., and S. Das (2001), Aftershock zones of large shallow earthquakes: fault dimensions, aftershock area expansion and scaling relations, *Geophysical Journal International*, *147*(2), 272–293, doi:10.1046/j.1365-246X.2001.00522.x.

Herrmann, R. B., L. Malagnini, and I. Munafo (2011), Regional Moment Tensors of the 2009 L'Aquila Earthquake Sequence, *Bulletin of the Seismological Society of America*, *101*(3), 975–993, doi:10.1785/0120100184.

Hsu, Y.-J., M. Simons, J.-P. Avouac, J. Galetzka, K. Sieh, M. Chlieh, D. Natawidjaja, L. Prawirodirdjo, and Y. Bock (2006), Frictional Afterslip Following the 2005 Nias-Simeulue Earthquake, Sumatra, *Science*, *312*(5782), 1921–1926, doi:10.1126/science.1126960.

Johnson, K. M., J. Fukuda, and P. Segall (2012), Challenging the rate-state asperity model: Afterslip following the 2011 M9 Tohoku-oki, Japan, earthquake, *Geophysical Research Letters*, *39*(20), L20,302, doi:10.1029/2012GL052901.

Jonsson, S., P. Segall, R. Pedersen, and G. Bjornsson (2003), Post-earthquake ground movements correlated to pore-pressure transients, *Nature*, *424*(6945), 179–83.

Jolivet, R., C. Lasserre, M.-P. Doin, S. Guillaso, G. Peltzer, R. Dailu, J. Sun, Z.-K. Shen, and X. Xu (2012), Shallow creep on the Haiyuan Fault (Gansu, China) revealed by SAR Interferometry, *Journal of Geophysical Research: Solid Earth*, *117*(B6), B06,401, doi:10.1029/2011JB008732.

Lavecchia, G., F. Ferrarini, F. Brozzetti, R. D. Nardis, P. Boncio, and L. Chiaraluce (2012), From surface geology to aftershock analysis: Constraints on the geometry of the L'Aquila 2009 seismogenic fault system, *Italian Journal of Geosciences*, *131*(3), 330–347, doi:10.3301/IJG.2012.24.

Lin, Y.-n. N., A. Sladen, F. Ortega-Culaciati, M. Simons, J.-P. Avouac, E. J. Fielding, B. A. Brooks, M. Bevis, J. Genrich, A. Rietbrock, C. Vigny, R. Smalley, and A. Socquet (2013), Coseismic and postseismic slip associated with the 2010 Maule Earthquake, Chile: Characterizing the Arauco Peninsula barrier effect, *Journal of Geophysical Research: Solid Earth*, *118*(6), 3142–3159, doi:10.1002/jgrb.50207.

Lohman, R. B., and M. Simons (2005), Some thoughts on the use of InSAR data to constrain models of surface deformation: Noise structure and data downsampling, *Geochemistry, Geophysics, Geosystems*, *6*(1), Q01,007, doi:10.1029/2004GC000841.

Luccio, F. D., G. Ventura, R. D. Giovambattista, A. Piscini, and F. R. Cinti (2010), Normal faults and thrusts reactivated by deep fluids: The 6 April 2009 Mw 6.3 L'Aquila earthquake, central Italy, *Journal of Geophysical Research: Solid Earth*, *115*(B6), doi: 10.1029/2009JB007190.

Lucente, F. P., P. D. Gori, L. Margheriti, D. Piccinini, M. D. Bona, C. Chiarabba, and N. P. Agostinetti (2010), Temporal variation of seismic velocity and anisotropy before the 2009 MW 6.3 L'Aquila earthquake, Italy, *Geology*, *38*(11), 1015–1018, doi: 10.1130/G31463.1.

Magnoni, F., E. Casarotti, A. Michelini, A. Piersanti, D. Komatitsch, D. Peter, and J. Tromp (2014), Spectral Element Simulations of Seismic Waves Generated by the 2009 L'Aquila Earthquake, *Bulletin of the Seismological Society of America*, *104*(1), 73–94, doi:10.1785/0120130106.

Mai, P. M., and K. K. S. Thingbaijam (2014), SRCMOD: An Online Database of Finite-Fault Rupture Models, *Seismological Research Letters*, *85*(6), 1348–1357, doi:10.1785/0220140077.

Malagnini, L., F. P. Lucente, P. D. Gori, A. Akinci, and I. Munafo' (2012), Control of pore fluid pressure diffusion on fault failure mode: Insights from the 2009 L'Aquila seismic sequence, *Journal of Geophysical Research: Solid Earth*, *117*(B5), doi:10.1029/2011JB008911.

Malservisi, R., S. Y. Schwartz, N. Voss, M. Protti, V. Gonzalez, T. H. Dixon, Y. Jiang, A. V. Newman, J. Richardson, J. I. Walter, and D. Voyenko (2015), Multiscale postseismic behavior on a megathrust: The 2012 Nicoya earthquake, Costa Rica, *Geochemistry, Geophysics, Geosystems*, *16*(6), 1848–1864, doi:10.1002/2015GC005794.

Marone, C. J., C. H. Scholtz, and R. Bilham (1991), On the mechanics of earthquake afterslip, *Journal of Geophysical Research: Solid Earth*, *96*(B5), 8441–8452, doi: 10.1029/91JB00275.

Miller, S. A., C. Collettini, L. Chiaraluce, M. Cocco, M. Barchi, and B. J. P. Kaus (2004), Aftershocks driven by a high-pressure CO_2 source at depth, *Nature*, *427*(6976), 724–727, doi:10.1038/nature02251.

Minson, S. E., M. Simons, and J. L. Beck (2013), Bayesian inversion for finite fault earthquake source models I: theory and algorithm, *Geophysical Journal International*, *194*(3), 1701–1726, doi:10.1093/gji/ggt180.

Miyazaki, S., P. Segall, J. Fukuda, and T. Kato (2004), Space time distribution of afterslip following the 2003 Tokachi-oki earthquake: Implications for variations in fault zone frictional properties, *Geophysical Research Letters*, *31*(6), L06,623, doi: 10.1029/2003GL019410.

Munekane, H. (2012), Coseismic and early postseismic slips associated with the 2011 off the Pacific coast of Tohoku Earthquake sequence: EOF analysis of GPS kinematic time series, *Earth, Planets and Space*, *64*(12), 3, doi:10.5047/eps.2012.07.009.

Nur, A., and G. Mavko (1974), Postseismic Viscoelastic Rebound, *Science*, *183*(4121), 204–206, doi:10.1126/science.183.4121.204.

Parzen, E. (1962), On Estimation of a Probability Density Function and Mode, *The Annals of Mathematical Statistics*, *33*(3), 1065–1076.

Peltzer, G., P. Rosen, F. Rogez, and K. Hudnut (1998), Poroelastic rebound along the Landers 1992 earthquake surface rupture, *Journal of Geophysical Research: Solid Earth*, *103*(B12), 30,131–30,145, doi:10.1029/98JB02302.

Peng, Z., and P. Zhao (2009), Migration of early aftershocks following the 2004 Parkfield earthquake, *Nature Geoscience*, *2*, 877–881, doi:10.1038/ngeo697.

Perfettini, H., and J.-P. Avouac (2004), Postseismic relaxation driven by brittle creep: A possible mechanism to reconcile geodetic measurements and the decay rate of aftershocks, application to the Chi-Chi earthquake, Taiwan, *Journal of Geophysical Re-*

search: Solid Earth, *109*(B2), B02,304, doi:10.1029/2003JB002488.

Perfettini, H., and J.-P. Avouac (2007), Modeling afterslip and aftershocks following the 1992 Landers earthquake, *Journal of Geophysical Research: Solid Earth*, *112*(B7), B07,409, doi:10.1029/2006JB004399.

Perfettini, H., and J. P. Avouac (2014), The seismic cycle in the area of the 2011 Mw9.0 Tohoku-Oki earthquake, *Journal of Geophysical Research: Solid Earth*, *119*(5), 4469–4515, doi:10.1002/2013JB010697.

Perfettini, H., W. B. Frank, D. Marsan, and M. Bouchon (2018), A Model of Aftershock Migration Driven by Afterslip, *Geophysical Research Letters*, *45*(5), 2283–2293, doi:10.1002/2017GL076287.

Pollitz, F. F., R. Burgmann, and P. Segall (1998), Joint estimation of afterslip rate and postseismic relaxation following the 1989 Loma Prieta earthquake, *Journal of Geophysical Research: Solid Earth*, *103*(B11), 26,975–26,992, doi:10.1029/98JB01554.

Pondrelli, S., S. Salimbeni, A. Morelli, G. Ekstrom, M. Olivieri, and E. Boschi (2010), Seismic moment tensors of the April 2009, L'Aquila (Central Italy), earthquake sequence, *Geophysical Journal International*, *180*(1), 238–242, doi:10.1111/j.1365-246X.2009.04418.x.

Ragon, T., A. Sladen, and M. Simons (2018), Accounting for uncertain fault geometry in earthquake source inversions - I: theory and simplified application, *Geophysical Journal International*, *214*(2), 1174–1190, doi:10.1093/gji/ggy187.

Rice, J., and A. L. Ruina (1983), *Stability of Steady Frictional Slipping*, vol. 50, doi:10.1115/1.3167042.

Rosen, P. A., S. Henley, G. Peltzer, and M. Simons (2004), Update Repeat Orbit Interferometry Package Released, *EOS Transactions*, *85*, 47–47, doi:10.1029/2004EO050004.

Ross, Z. E., C. Rollins, E. S. Cochran, E. Hauksson, J.-P. Avouac, and Y. Ben-Zion (2017), Aftershocks driven by afterslip and fluid pressure sweeping through a fault-fracture mesh, *Geophysical Research Letters*, *44*(16), 2017GL074,634, doi:10.1002/2017GL074634.

Salman, R., E. M. Hill, L. Feng, E. O. Lindsey, D. Mele Veedu, S. Barbot, P. Banerjee, I. Hermawan, and D. H. Natawidjaja (2017), Piecemeal Rupture of the Mentawai Patch, Sumatra: The 2008 Mw 7.2 North Pagai Earthquake Sequence, *Journal of Geophysical Research: Solid Earth*, *122*(11), 9404–9419, doi:10.1002/2017JB014341.

Scognamiglio, L., E. Tinti, and A. Michelini (2009), Real-Time Determination of Seismic Moment Tensor for the Italian Region, *Bulletin of the Seismological Society of America*, *99*(4), 2223–2242, doi:10.1785/0120080104.

Scuderi, M. M., and C. Collettini (2016), The role of fluid pressure in induced vs. triggered seismicity: insights from rock deformation experiments on carbonates, *Scientific Reports*, *6*, 24,852, doi:10.1038/srep24852.

Segall, P. (2010), *Earthquake and Volcano Deformation*, Princeton University Press, google-Books-ID: x6Fp4hMBTpYC.

Serpelloni, E., L. Anderlini, and M. E. Belardinelli (2012), Fault geometry, coseismic-slip distribution and Coulomb stress change associated with the 2009 April 6,Mw 6.3, L'Aquila earthquake from inversion of GPS displacements, *Geophysical Journal International*, *188*(2), 473–489, doi:10.1111/j.1365-246X.2011.05279.x.

Sladen, A., H. Tavera, M. Simons, J. P. Avouac, A. O. Konca, H. Perfettini, L. Audin, E. J. Fielding, F. Ortega, and R. Cavagnoud (2010), Source model of the 2007 Mw 8.0 Pisco, Peru earthquake: Implications for seismogenic behavior of subduction megathrusts, *Journal of Geophysical Research: Solid Earth*, *115*(B2), B02,405, doi:10.1029/2009JB006429.

Smith, B., and D. Sandwell (2004), A three-dimensional semianalytic viscoelastic model for time-dependent analyses of the earthquake cycle, *Journal of Geophysical Research: Solid Earth*, *109*(B12), B12,401, doi:10.1029/2004JB003185.

Terakawa, T., A. Zoporowski, B. Galvan, and S. A. Miller (2010), High-pressure fluid at hypocentral depths in the L'Aquila region inferred from earthquake focal mechanisms, *Geology*, *38*(11), 995–998, doi:10.1130/G31457.1.

Trasatti, E., C. Kyriakopoulos, and M. Chini (2011), Finite element inversion of DInSAR data from the Mw 6.3 L'Aquila earthquake, 2009 (Italy), *Geophysical Research Letters*, *38*(8), L08,306, doi:10.1029/2011GL046714.

Valoroso, L., L. Chiaraluce, D. Piccinini, R. Di Stefano, D. Schaff, and F. Waldhauser (2013), Radiography of a normal fault system by 64,000 high-precision earthquake locations: The 2009 L'Aquila (central Italy) case study, *Journal of Geophysical Research: Solid Earth*, *118*(3), 1156–1176, doi:10.1002/jgrb.50130.

Vittori, E., P. D. Manna, A. M. Blumetti, V. Comerci, L. Guerrieri, E. Esposito, A. M. Michetti, S. Porfido, L. Piccardi, G. P. Roberts, A. Berlusconi, F. Livio, G. Sileo, M. Wilkinson, K. J. W. McCaffrey, R. J. Phillips, and P. A. Cowie (2011), Surface Faulting of the 6 April 2009 Mw 6.3 L'Aquila Earthquake in Central Italy, *Bulletin of the Seismological Society of America*, *101*(4), 1507–1530, doi:10.1785/0120100140.

Volpe, M., A. Piersanti, and D. Melini (2012), Complex 3-D Finite Element modelling of the 2009 April 6 L'Aquila earthquake by inverse analysis of static deformation, *Geophysical Journal International*, *188*(3), 1339–1358, doi:10.1111/j.1365-246X.2011.05330.x.

Volpe, M., S. Atzori, A. Piersanti, and D. Melini (2015), The 2009 L'Aquila earthquake coseismic rupture: open issues and new insights from 3d finite element inversion of GPS, InSAR and strong motion data, *Annals of Geophysics*, *58*(2), S0221, doi:10.4401/ag-6711.

Wang, L., S. Hainzl, G. Zoller, and M. Holschneider (2012), Stress- and aftershock-constrained joint inversions for coseismic and postseismic slip applied to the 2004 M6.0 Parkfield earthquake, *Journal of Geophysical Research: Solid Earth*, *117*(B7), B07,406, doi:10.1029/2011JB009017.

Yano, T. E., G. Shao, Q. Liu, C. Ji, and R. J. Archuleta (2014), Coseismic and potential early afterslip distribution of the 2009 Mw 6.3 L'Aquila, Italy earthquake, *Geophysical Journal International*, *199*(1), 23–40, doi:10.1093/gji/ggu241.

Zhu, L., and L. A. Rivera (2002), A note on the dynamic and static displacements from a point source in multilayered media, *Geophysical Journal International*, *148*(3), 619–627, doi:10.1046/j.1365-246X.2002.01610.x.